Chapter 2

Transmission of Tidal Stresses by Ice Streams

Geodetic surveys suggest that ocean tides can modulate the motion of Antarctic ice streams. Data from Whillans Ice Plain, Rutford Ice Stream, and other Antarctic ice streams show periodicity in flow velocity at periods similar to those of ocean tides at geodetic stations many tens of kilometers inland from the grounding line. These data suggest that ocean tidal stresses can perturb ice stream motion about an order of magnitude farther inland than tidal flexure of the ice stream alone. Recent models exploring the role of tidal perturbations in basal shear stress are all two dimensional e.g., Anandakrishnan and Alley, 1997; Bindschadler et al., 2003; Gudmundsson, 2006, 2007, 2011; Sergienko et al., 2009; Winberry et al., 2009; Walker et al., 2012), with the impact of the ice stream margins either ignored or parameterized. In this chapter, we use two- and three-dimensional finite element modeling to investigate the transmission of tidal stresses in ice streams and the impact of considering more realistic, three-dimensional, ice stream geometries. We demonstrate that the assumption that elastic tidal stresses in ice streams propagate large distances inland fails for channelized glaciers. The resistance at the ice stream margins causes an intrinsic, exponential decay in the tidal stress. This stress decay occurs even with an unrealistic frictionless basal condition beneath the ice stream and even then, does not fit observations from the aforementioned Antarctic ice streams.

2.1 Introduction

All ice streams respond to the daily fluctuations in ocean tidal height. The spatial and temporal extent of this tidal response varies dramatically between ice streams, as demonstrated by surface observations discussed earlier in section 1.3. At one extreme are the outlet glaciers of Greenland and some ice streams of Antarctica, which have only surface movement affected by the ocean tides over horizontal distance inland of the grounding line comparable to a few ice-thicknesses (1 ice-thickness ranges from 600 meters to 2 kilometers for our purposes). In constrast, many of the major ice streams of the Siple Coast (Whillans, Bindschadler, and Kamb Ice Streams) and the Rutford Ice Stream, exhibit surface motion influenced by tides many tens of ice-thicknesses inland of their respective grounding lines. As this latter behavior is anomalous, these ice streams are the focus of this chapter.

Many two-dimensional models are capable of reproducing the seemingly inordinate influence that the ocean tides have on the motion of some Antarctic ice streams (e.g., Anandakrishnan and Alley, 1997; Bindschadler et al., 2003; Gudmundsson, 2006, 2007, 2011; Sergienko et al., 2009; Winberry et al., 2009; Walker et al., 2012). Given that the Maxwell relaxation time (T_{max}) for ice is on the order of hours for tidal loads, these models call on either elastic or viscoelastic transmission of tidal loading stresses through the ice stream to drive the observed ice motions. We discuss several representative published models with the aim of understanding the assumptions made about the upstream transmission of tidal stresses.

A standard approximation for glacial flow is the *flow-line model.* A flow-line model is a two-dimensional representation of a vertical slice along the glacier's flow-

direction, with any resistive forces in the third dimension ignored. The underlying assumption of such a formulation requires that only the conditions at the ice stream's bed determine the sliding and flow behavior of the entire ice stream. Such a model is only appropriate for ice "far" from the lateral margins of the ice stream. The spatially-averaged shear stress formulations of Bindschadler et al. (2003) and Winberry et al. (2009) use flow-line models to investigate the tidally-perturbed surface displacements of Rutford and Whillans Ice Streams. These models assume that tidal stress is uniformly distributed over the entire ice stream and that the stress is completely supported by the ice stream's base. The result is a length-scale for the transmission of stress that depends completely on the length of the ice stream assumed in the problem.

Finite element analysis in two-dimensions allows for flow-line models with increased complexity and realistic geometries. An early example of this approach is the modeling of Anandakrishnan and Alley (1997), which assumes the ice stream behaves as a two-dimensional elastic body (in cross section) riding over a viscous bed. Anandakrishnan and Alley (1997) find that a stress applied at the grounding line decays exponentially with distance inland. The decay of this "tidal" load is controlled primarily by the properties of the viscous till layer in this model, namely the ratio of effective viscosity of the till to the thickness of the till.

Of the published modeling after Anandakrishnan and Alley (1997), the two most applicable models of tidal stress propagation are those of Gudmundsson (2011) and Walker et al. (2012). Both are two-dimensional flow-line models incorporating nonlinear viscoelasticity and a nonlinear basal sliding law. The response of the modeled ice stream is found to relate directly to the basal boundary condition. This result is intuitive as any

resistance due to the lateral margins of the ice is neglected for a flow-line model, and thus the model ice stream's response to a tidal load must be controlled by rheological character of the stream's bed alone. These models do not, however, demonstrate that the lateral resistance in these ice streams is indeed negligible.

Sergienko et al. (2009) approximates an ice stream as a series of masses (blocks) connected elastically (by springs) and restrained laterally (by further springs), under the action of an applied shear along a frictional basal contact. Unlike the flow-line models discussed previously, this spring-block model incorporates the lateral resistance of the ice margins. In this model, Sergienko et al. (2009) note that a "tidal" load applied at one edge diminishes with distance from the loaded block, but this stress decay is not explored in any detail. Intuitively, this transmission distance depends on the stiffness of the springs, both between the masses and as lateral restraints, as well as the magnitude of the basal friction imposed in the model. However, there is no obvious relationship between a physical length-scale and the number of blocks and springs in the model, and it is not clear if the decay of the tidal stress is caused by marginal or basal resistance, or both.

2.2 Methodology

As our brief review of the published literature shows, there is a dearth of three-dimensional ice stream models exploring the transmission of a tidal load inland of the grounding line that account for the resistance of the ice stream's lateral margins. To explore the role of an ice stream's lateral margins, we present results from two- and three-dimensional elastic models that explore and quantify the role that the three-dimensional ice stream geometry plays in controlling transmission of tidal stresses. The opening portion of this methodology section describes the conceptual configuration of

our models, which are shown schematically in figure 2.1. The methods section then closes with a brief description of the finite element modeling necessary to create these models.

2.2.1 Model Descriptions

We begin with a two-dimensional linear elastic flow-line model (figure 2.1A). As with all flow-line models, the underlying assumption is that the ice stream is infinite and uniform in the third dimension, such that there effectively are no lateral margins to the ice stream. These simplified models establish the expected "end-member" behavior of an elastic ice stream with extreme basal conditions of either a fully frozen (no-slip) bed or a freely sliding (no shear traction) bed. Additionally, these two-dimensional models investigate the role played by an ice shelf as the intermediary between the ocean tides and the grounded ice stream (see Appendix 2A).

Based on the insight gained from these two-dimensional models, we then move to our three-dimensional models (figure 2.1B), studying the impact of resistive shearing at the lateral margins of an ice stream on the upstream transmission of the applied tidal load. The ice stream is defined in these models as a block of ice "sliding" over a frictionless basal boundary with lateral margins consisting of two blocks of ice that are "frozen" to their beds. Such models investigate the role that the overall geometry of the ice stream (i.e., ice stream width and thickness) has on the transmission of the stress inland of the grounding line.

2.2.2 Model Construction

We use the finite element software *Pylith* (Williams et al., 2005; Williams, 2006; Aagaard et al., 2007; 2008; 2011) and meshing software *Cubit* (`cubit.sandia.gov`)

for our computational modeling. As the general finite element formulation has already been discussed section 1.5, we only describe the mesh geometries and boundary conditions used in our two- and three-dimensional models here.

Our default two-dimensional model is two hundred kilometers long and one kilometer thick. For all our modeling, if the model is long compared to the other dimension, the length is not a controlling parameter. As the bottom corner of the axial forced edge is a location of stress concentration, we refine our mesh near this point to improve our model stability, resulting in a variable element length in the vertical and horizontal directions. In our three-dimensional model, we apply the same mesh-refinement scheme in the vertical and longitudinal direction; in the transverse direction, we refine the elements corresponding to the ice stream and then gradationally increase the element length away from the ice stream margin. The extent of the non-sliding area is chosen to be large enough that changing its width does not impact the behavior of the ice stream proper.

The basal boundary condition is either a Dirichlet condition with zero-displacement in all directions ("frozen") or a Robin condition with no vertical displacements and zero shear traction ("sliding"). The tidal stress change is a normal force of magnitude equal to the hydrostatic pressure ($\rho g \Delta h$ where Δh is the amplitude of the tide). For the two-dimensional models with an ice shelf, the tidal load acts normal to the base and vertical edge of the ice shelf. For the two-dimensional models with no shelf and the three-dimensional models, the tidal load acts on the vertical edge of the ice stream at the grounding line. In these latter models, neglecting the ice shelf is justifiable as the presence of a shelf only perturbs the stresses in the ice stream near the grounding

line, and our interest is in the stresses far inland of the grounding line. See appendices 2A and 2B for an extended discussion of the impact of the ice shelf on our models. Lastly, in these linear elastic models, it is not necessary to explicitly vary the loading through time, as our solutions must necessarily vary linearly with the magnitude of the applied load.

Table 2.1 lists the default rheological parameters used in our finite element modeling presented in this chapter. Note that while Young's modulus is varied throughout many of our models, all quantities marked with a "+" are fixed throughout all the simulations. Apart from linear elasticity, our most important rheological assumption is that the Poisson's ratio, ν, is well constrained by laboratory experiments (e.g., Gammon et al., 1983A; 1983B; Patrenko and Whitford, 2002).

2.3 Results

PyLith calculates the full stress and strain tensors, as well as displacement and velocity vectors, at every node of our model mesh. As we ran close to two dozen models, we show only representative results in the main chapter (figures 2.2 to 2.7). Tables 2.3 and 2.4 list important quantities from all the models, while appendix 2C shows the stress and displacement profiles for all our two-dimensional models and appendix 2D shows the stress field for the three-dimensional models. Note that while we model only physically-representative geometries in our parameter exploration, in order to quantify the dependence of the model on Young's modulus, we include models with Young's moduli an order of magnitude larger and smaller than the value from Patrenko and Whitford (2002). While such values may be unrealistic for ice, the wide range of values allows us to easily distinguish the effects of changing the elasticity of each model.

Lastly, to aid in comparing the stress magnitude between models, we define an equivalent stress, τ_{eq}, based on the Von Mises criterion. τ_{eq} is defined in two and three dimensions as:

$$\text{2D: } {\tau_{eq}}^2 = \frac{1}{2}\left[\left(\sigma_{xx} - \sigma_{yy}\right)^2 + {\sigma_{xx}}^2 + {\sigma_{yy}}^2 + 6 * {\sigma_{xy}}^2\right] \quad (2.1A)$$

$$\text{3D: } {\tau_{eq}}^2 = \frac{1}{2}\left[\left(\sigma_{xx} - \sigma_{yy}\right)^2 + \left(\sigma_{yy} - \sigma_{zz}\right)^2 + (\sigma_{xx} - \sigma_{zz})^2 + 6\left({\sigma_{xz}}^2 + {\sigma_{xy}}^2 + {\sigma_{yz}}^2\right)\right] \quad (2.1B)$$

2.3.1 Two-Dimensional Results

The stress distributions from our two-dimensional models with free-sliding and frozen basal boundary conditions are shown in figures 2.2 and 2.3, respectively. In both panels A and B of these figures, the left column plots the stress results for models including an ice shelf, while the right column plots results for models with only axial forcing. In panel A, the figure shows superimposed longitudinal profiles of τ_{eq} taken at depth intervals of 10 meters. In panel B, the logarithm of the absolute value of the three in-plain stress components is plotted for the entire two-dimensional model domain.

In most models, the magnitude of stress within our body decays exponentially with distance from the grounding line (at x=0). Only in the model with a sliding bed and axial forcing (figure 2.2, right column) does the axial stress not decay with inland distance. We define a stress-transmission length-scale, L_{tr}, as the distance inland of the grounding line over which the tidal stress drops by one order of magnitude. Table 2.2 summarizes L_{tr} for all stress components for the four models shown in figures 2.2 and 2.3.

For both basal boundary conditions, the solution for the model with the ice shelf approaches the solution of the shelf-free model after about five ice-thicknesses. For the free-sliding model, the flexural stresses also decay with distance inland of the grounding line, following the expected functional form of a sinusoid multiplied by an exponential function (e.g., Turcotte and Schubert, 2002). The first wavelength of this sinusoid can be seen in figure 2.2A, with a zero crossing approximately two kilometers inland (i.e., left) of the grounding line. Beyond approximately five kilometers inland of the grounding line, the two models behave identically. For the model with a frozen bed (figure 2.3), flexural and axial stresses decay exponentially with distance inland of the grounding line with similar decay rates. The influence of the ice shelf on the deformation near the grounding line is explored more fully in appendices 2A and 2B.

Not surprisingly, the displacement field in our two-dimensional models mirrors the stress field, as figure 2.4 demonstrates for the ice shelf models. Panel A shows the displacement results for the model with a sliding bed, while panel B shows the results for a model with a frozen bed. In each panel, the mesh is warped by the displacement values exaggerated by a factor of 1000 for the sliding base model and 50,000 for the frozen base model. This figure is useful to determine the general character of the displacement field, which also exhibits an exponential decay with distance inland of the grounding line. Linear elasticity predicates that the decay of displacements matching that of the stress. Thus, the same L_{tr} in tables 2.3 and 2.4 calculated for the stress also represents the behavior of the displacements.

2.3.2 Three-Dimensional Results

Figure 2.5 shows the values of τ_{eq} from a representative three-dimensional model that is one kilometer thick and ten kilometers wide. Each line represents horizontal profiles taken at a ten meter depth interval and a transverse spacing of one kilometer. The stress decays exponentially at approximately the same rate regardless of the *Y* or *Z* coordinates chosen. Recall that the ice stream in our three-dimensional model slides frictionless along the bed; thus, the exponential decay of stress within the three-dimensional ice stream is clearly different from the constant stress behavior of our free-sliding two-dimensional model. The presence of the lateral margins of the ice stream alone induces an exponential decay of the stresses in the ice stream as a function of distance inland of the grounding line.

Figure 2.6 shows the full basal stress field (i.e., the six independent stress components) of the representative three-dimensional model. Only the longitudinal normal stresses (σ_{xx}), transverse normal stresses (σ_{yy}), and the shear due to the sidewalls (σ_{xy}) are nonzero beyond a distance of a few kilometers from the forced edge. The other stress components are direct consequences of stress concentration at the transition from no slip to sliding ice at the base, and decay rapidly with distance from both the margins and the grounding line. Note that the lack of basal friction accounts for the lack of basal shear stresses (σ_{yz} and σ_{xz}).

Figure 2.7 shows a view of the three-dimensional mesh with a stream width of five kilometers, warped by the displacement vector magnitude multiplied by a factor of 500,000. The fixed basal condition beneath the lateral margins of the ice stream clearly has a strong influence on the displacement field, which follows a polynomial profile in

plan-view. Such a displacement field is akin to the solution to for an elastic (Bernoulli-Euler) beam under a constant pressure that is simply supported at both edges (e.g., Turcotte and Schubert, 2002). Additionally, recall that the displacements in our three-dimensional models decay exponentially with inland distance at the same rate that the stress signal decays due to the elastic rheology of the ice.

2.4 Transmission of Tidal Stresses

As seen in all models with either basal or lateral stress resistance, the tidal stresses decay exponentially with distance inland of the grounding line. We use $L_{tr,}$ the stress-transmission length-scale, as a direct measure of the inland extent of tidal influence on the motion of an ice stream. Throughout the remaining discussion in this chapter, we estimate L_{tr} using τ_{eq}, as the value of L_{tr} calculated from the equivalent stress matches the longest L_{tr} derived from the individual stress components (see table 2.2). Table 2.3 and 2.4 show the value of L_{tr} for many different combinations of geometry and elastic moduli for the two- and three-dimensional models, respectively. For the two-dimensional models, we vary *h* and *E* while for the three-dimensional models we vary *h*, *w*, and *E*.

Using the information found in tables 2.3 and 2.4, figures 2.8 and 2.9 show the full variability of our solutions with the geometric and rheological parameters in our models. Increasing the size of the model domain (i.e., *h* and *w*) and the amplitude of the applied load increases the value of the stress, while displacements vary proportionally to the applied load and inversely to Young's modulus. However, only the geometric parameters determine the value of the stress decay (as evidenced by the constant value of L_{tr} for models of the same geometry). For our two-dimensional model (with a frozen

bed), L_{tr} varies linearly with thickness. For our three-dimensional model, L_{tr} increases nonlinearly with increasing thickness and width.

We adopt an empirical functional form describing the relationship between stresses, displacements, and model parameters using the aforementioned model results. For the two-dimensional model, we find:

$$\begin{aligned} \sigma(x,z) &= \tilde{\sigma}_{GL}(h,z) \cdot \overline{\Delta h} \cdot 10^{-x\frac{\bar{h}}{\tilde{L}_{tr}}} \\ u(x,z) &= \tilde{u}_{GL}(h,z) \cdot \frac{\overline{\Delta h}}{\bar{E}} \cdot 10^{-x\frac{\bar{h}}{\tilde{L}_{tr}}} \end{aligned} \tag{2.2}$$

$\tilde{\sigma}_{GL}$ and $\tilde{u}_{GL}$ are, respectively, the centerline basal stress and surface displacement at the grounding line for reference model one kilometer thick with a one meter tidal load using the value of 9.33 GPa for E. $\tilde{L}_{tr}$ is the transmission length-scale for the reference model, $\bar{E}$ is the normalized Young's modulus with respect to the canonical value, $\bar{h}$ is the normalized model thickness with respect to one kilometer, and $\overline{\Delta h}$ is the normalized tidal height with respect to a one meter tide. Recall that as ρ and g are held constant, $\overline{\Delta h}$ really reflects a change in tidal load, and thus is a characteristic change in loading rather than a characteristic length-scale. For the three-dimensional models, the empirical forms of stress and displacement are:

$$\begin{aligned} \sigma(x,y,z) &= \tilde{\sigma}_{GL}(y,z,h,w) \cdot \overline{\Delta h} \cdot 10^{\frac{-x}{\tilde{L}_{tr}(h,w)}} \\ u(x,y,z) &= \tilde{u}_{GL}(y,z,h,w) \cdot \frac{\overline{\Delta h}}{\bar{E}} \cdot 10^{\frac{-x}{\tilde{L}_{tr}(h,w)}} \end{aligned} \tag{2.3}$$

These results indicate that the distribution of stresses depends only on model loading style and geometry, and are completely independent of the elastic properties of the model, assuming the Young's modulus for the ice is homogenous.

From comparing the model results in table 2.4, a rough rule of thumb is that L_{tr} is between 1.2 and 1.5 times the width of the ice stream and only increases slightly with increasing ice stream thickness in our three-dimensional models. Thus, tidal stresses at a distance inland of the grounding line equal to 2.5 times the ice stream width, there should be no tidal influence on the ice stream motion. For our models of Bindschadler and Rutford Ice Streams, this rough rule of thumb suggests that the tidal influence should die out at 100 kilometers and 75 kilometers, respectively, (flagged models in Table 4; mesh sizes shown in figure 2.10). However, figure 2.11 demonstrates that even this decay is too severe to match the maximum observed displacement at stations inland of the grounding line (GPS data reported in Anandakrishnan et al., 2003; Gudmundsson, 2007 and provided by S. Anandakrishnan and H. Gudmundsson).

Note that for Bindschadler Ice Stream, the grounding line curls along the edge of the ice stream for almost 75 kilometers. The modeled trend in figure 2.11 ignores this feature, which is a clear simplification of the model geometry. From our simple models, we find that the effective ice stream width would have to be over 250 kilometers for the model decay rates to match the observations. While a more representative geometry would result in a better approximation of the value of L_{tr} (a value that is likely different for the convergence zone of Bindschadler and MacAyeal Ice Streams and Bindschadler Ice Stream proper), our modeling suggests that an elastic model of Bindschadler Ice Stream cannot reproduce the decay length-scale observed by Anandakrishnan et al. (2003).

Of course, real ice streams are neither frozen to nor sliding frictionlessly over their beds. Frictional sliding plays a major role in determining the ice stream's total flow

(e.g., Weertman, 1957; 1964; Engelhardt and Kamb, 1998; Hughes, 1998; Cuffey and Paterson, 2010). The values of L_{tr} from our frozen bed two-dimensional models should be considered as a minimum value for frozen bed flow-line models, while our three-dimensional models should be taken as maximum values as we assume frictionless sliding in our models. As our three-dimensional models predict a tidal influence that decays too rapidly to match observations when the base is frictionless, we conclude that a homogenous elastic ice stream is not capable of transmitting tidal stresses the many tens of kilometers inland that have been observed.

2.5 Discussion

As our results, along with those of Sergienko et al. (2009) and Anandakrishnan and Alley (1997), predict an exponential decay of stress while many other researchers found no such exponential decay of a tidal load (e.g., Bindschadler et al., 2003; Gudmundsson, 2011; Walker et al., 2012; Winberry et al., 2009), our discussion begins with this inconsistency in modeling results. After establishing that exponential decay of a tidal load is the expected result, we then discuss how our modeling compares to, and in many cases, refutes the results of other published models. Our discussion concludes by considering the shortcomings of our modeling as a motivation of chapter 3 of this thesis.

2.5.1 Comparison to Previous Models

St. Venant's Principle states that the influence of an applied load on an elastic body is negligible at great distances away from the applied load (e.g., Goodier, 1942; Timoshenko and Goodier, 1982) A clear extension of this principle is that an external load should decay rapidly when near a fixed edge. For instance, Goodier (1942) demonstrates that an axially forced block, when restrained from below, has a stress field

that is only important local to the edge of the applied load. Additionally, Goodier establishes the same conclusion when the block is fixed from both above and below. These two cases are identical to our two-dimensional model with a fixed base and the two-dimensional version (in map view) of our three-dimensional ice stream model, respectively. Timoshenko and Goodier (1982) provide an explicit form of the stress solution for similar, albeit not identical, models. In their article 24, Timoshenko and Goodier describe the expectation of exponential decay of stress with distance away from a point load applied to the opposite edges of a beam.

Comparing our present results to those of Anandakrishnan and Alley (1997), our two-dimensional model results represent extremes of Anandakrishnan and Alley's model. Our frozen bed model corresponds to Anandakrishnan's and Alley's model with either a zero-thickness viscous layer or an infinitely viscous ($\eta \approx \infty$) layer. Our sliding bed model corresponds to Anandakrishnan and Alley's model with an infinitely weak ($\eta \approx 0$) viscous layer. Our models bracket those of Anandakrishnan and Alley where two-layer models have the additional free parameter of till viscosity. Anandakrishnan and Alley's models can either constrain the viscosity of the viscous till layer using the transmission length of stress, or constrain the transmission length of stress using the till viscosity, but not both simultaneously. Additionally, the lack of lateral restraint in the model allows the physically unrealistic case of infinite stress-transmission. The same issue is present in all the flow-line models, and as such, the two-dimensional assumption of negligible lateral resistance is not physically realistic for ice streams.

Of all the published models, Sergienko et al. (2009) is the only study to explicitly account for lateral resistances. Removing the basal drag condition from Sergienko et

al.'s model results in a one-dimensional approximation of our three-dimensional modeling. However, the lack of a length-scale relationship for the elastic springs in Sergienko et al.'s model is a major deficiency in using the Sergienko et al.'s model to help constrain a stress-transmission length-scale. As our finite element modeling shows, the presence of non-sliding lateral margins and a zero-sliding basal condition both result in exponential decay of a tidal load with distance inland of the grounding line. Thus over the stick-slip cycle in Sergienko et al.'s paper, we expect that the stress-transmission would cycle between a thickness-controlled value when stuck and a width-controlled value when slipping.

2.5.2 Model Shortcomings

Our models are, by design, geometrically and rheologically simple. Even in our simple box models, the stress supported by the lateral margins directly controls the transmission of a tidal load on ice streams. Extending these results, models with a realistic geometry will vary substantially from the equivalent box model approximation only if the real ice stream's width changes dramatically along the flow direction. For channelized ice streams like Bindschalder and Rutford Ice Streams, the width of either ice stream does not change significantly through the region with CGPS observations (e.g., figure 2.10). For the Whillans Ice Plain, the extreme width of the unconfined ice plain (~ 100 kilometers wide) suggests that our channelized three-dimensional model may not be a good representation of this one ice stream.

To address the Whillans Ice Plain, we ran a constant-thickness model approximating the geometry of the ice plain, as shown in figure 2.13. For this model, we selected the location of the non-streaming ice by using RadarSAT imagery (from

nsidc.org) to determine the location of shear margins, where the basal boundary condition was fixed in all directions. The grounding line was matched to that found by Brunt et al. (2010), and an axial-only tidal load was applied normal to the entire length of the grounding line. The model also included a portion of ice shelf solely to increase the rate of convergence of our model. Having an explicit ice shelf in the model prevents the possibility of an unphysical buckling mode along the grounding line. The rate of convergence is increased by several orders of magnitude while having no effect on the stress state within the grounded ice.

As seen in figure 2.13, the stress decays exponentially with distance inland of the grounding line as expected from our other three-dimensional modeling. Due to the variable position and angle of the grounding line, the reference-frame independent stress components are more characteristic of the stress state for this model, demonstrating that the general stress pattern follows that of the channelized ice stream models. Shear stresses peak near the transition from stuck to sliding ice, as locally there are large shear stresses in the vertical direction. Across the main body of the ice plain, the octahedral shear stress is dominated by shear along the horizontal plane. The overall stress state is dominated by the normal component of the tidal load. L_{tr} in this model ranges from 50 to 125 kilometers, meaning that over the ice plain itself, tidal loading is fairly well transmitted over the ice plain. Note that the magnitude of stress drops rapidly in Mercer and Whillans Ice Streams, with the decay rate controlled by the ice stream width, as expected. In these cases, the values of L_{tr} are about 45 kilometers and 30 kilometers, respectively. Thus, only in the case of a very wide, unconstrained ice stream, elastic stress may be transmitted far upstream; however, for ice streams with a more common

channel morphology, incorporating a more realistic model geometry is unlikely to have a major impact on the transmission of stress.

The models presented thus far adopt a homogeneous linear elastic rheology, which is not the most realistic material model for ice. In the next chapter, we discuss two modifications to the rheological model for ice streams: strain-weakening within the lateral shear margins of the ice stream and nonlinear viscoelastic rheology to account for the interplay of viscous and elastic deformation at short timescales.

A final major simplification of our modeling is the lack of a frictional basal boundary. Instead we explored either zero displacement or zero friction basal condition. Our free slip three-dimensional models and our two-dimensional frozen bed models bookend the expected behavior of a fractional bed and thus adding basal friction will cause the transmission length-scale of a tidal load to range from that controlled primarily by the ice stream width for low friction to that controlled primarily by the ice stream thickness for high friction. As ice streams are wider than they are thick, we expect that friction hinders, rather than enhances, the transmission of a tidal stress.

The exception to the frictional reduction of the transmission length-scale would be if the slow-moving ice that buttresses the ice stream on the sides slides frictionally instead of being fixed at the bed. Should this be the case, the stress-transmission length-scale for a given model will be larger than we predict here. The overall effect would be equivalent to having a larger effective width of the ice stream. In the case of Antarctica, the role of basal sliding in the ice stream itself, or for the slow-moving marginal ice, is negligible due to the small driving stress, as discussed in section 1.5. We note that in the case of the ice-rock margins of the fjord-bounded Greenland outlet glaciers discussed in

chapter 1, the ice stream does slide along the lateral margins; however, the fairly rapid decay of tidal stresses with distance inland of the grounding line suggests the such an effect is limited at best.

2.6 Summary and Conclusions

The models presented here draw into question the hypothesis that the observed influence of ocean tides on ice stream motion occurs as elastic transmission through the bulk of the ice stream itself. This result implies one of two possible conclusions: one, that there is a mechanism, not explored here, that almost completely decouples the ice stream from its shear margins, essentially reducing the lateral support of the ice stream to nearly zero; or two, that a mechanism external to the ice stream bulk is necessary to explain the tidal component of ice stream motion. The uniform flow-line models which are the current state-of-the-art, implicitly assume the first. Our models demonstrate that the ice streams considered here are not wide "enough" to neglect the resistance of the lateral margins. Furthermore, even the name "shear margins" implies that there is an amount of lateral support sufficient to induce shear in the ice stream's margins, making large-scale decoupling improbable.

We conclude that a mechanism external to the ice stream bulk underlies the transmission of ocean tidal loading far inland of the grounding line. While not explored here, our preferred hypothesis is that the ocean tides perturb the stress balance at the ice-bed interface through the subglacial hydrologic network. Any further discussion of such a process relies on quantifying the spatial extent that ocean tides are 'felt' through the subglacial hydrologic network, which is beyond the scope of this paper.

	Variable Names	**Units**
E	Young's modulus	Pa
g	Gravitational acceleration	m s^{-2}
H	Ice stream thickness	m
Δh	Tide amplitude	m
L_{tr}	Stress-transmission length-scale	km
$\tilde{L}_{tr}$	Reference stress-transmission length-scale	km
T_{max}	Maxwell relaxation time	S
$\tilde{u}_{GL}$	Centerline displacement magnitude at the grounding line	cm
w	Ice stream width	km
η	Viscosity	Pa s
ν	Poisson's ratio	--
ρ	Ice density	kg m^{-3}
σ_{ij}	Stress component	Pa
$\tilde{\sigma}_{GL}$	Centerline stress magnitude at the grounding line	Pa
σ_{tide}	Tidal stress	Pa
τ_{eq}	Equivalent (Von Mises) stress	Pa
"$\bar{}$"	Normalized quantity	

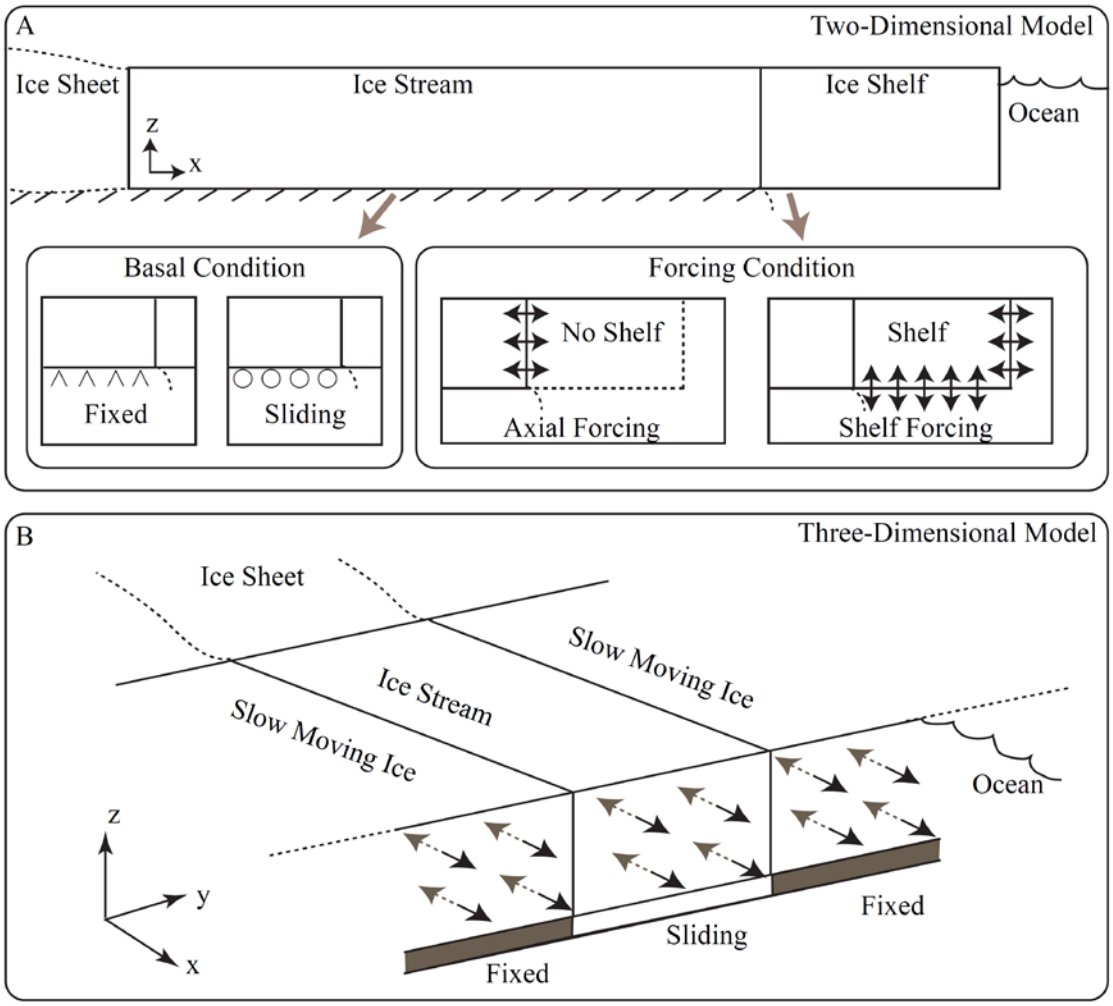

Figure 2.1: Schematics of the models used in this chapter. Inset boxes show options used in each model. For the two-dimensional models, these options are either a fixed ($u_x = u_y = u_z = 0$) or sliding ($u_z = 0$) basal condition, and either a pure axial loading condition or a shelf model. The three-dimensional model assumes a uniform, isotropic value for the Young's modulus throughout the entire domain.

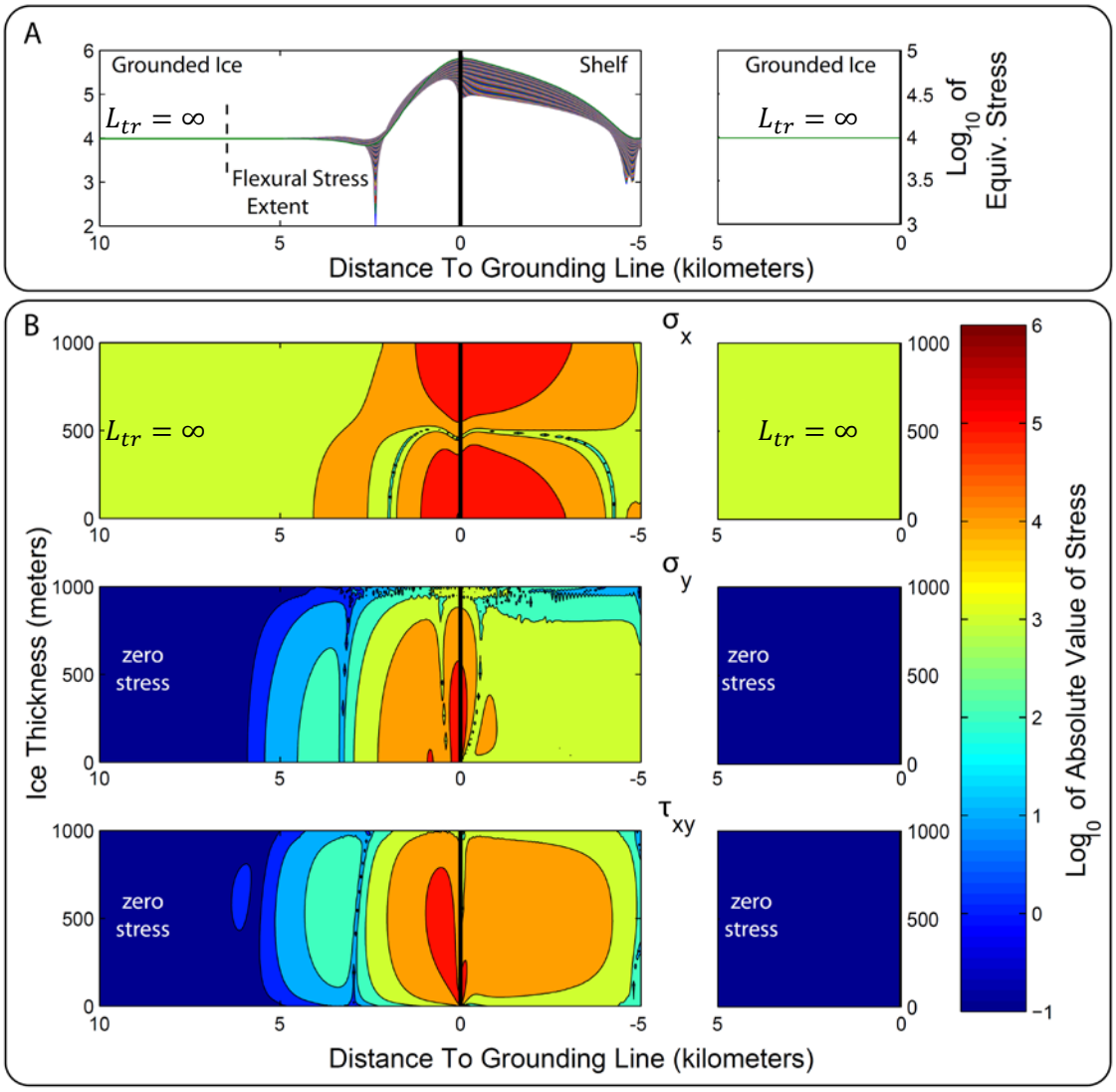

Figure 2.2: Distributions of stress for a two-dimensional model with frictionless basal sliding. Panel A shows profiles of longitudinal τ_{eq} profiles at a depth interval of 10 meters, while panel B shows the σ_x, σ_y, and τ_{xy} components of stress. The left column for both panels shows a model with an ice shelf; the right column for both panels shows a model with no ice shelf and only an axial loading. In these frictionless models, axial stress does not decay with distance and flexural stress rapidly decays near the grounding line. L_{tr} is the stress decay length, and is defined in the main text.

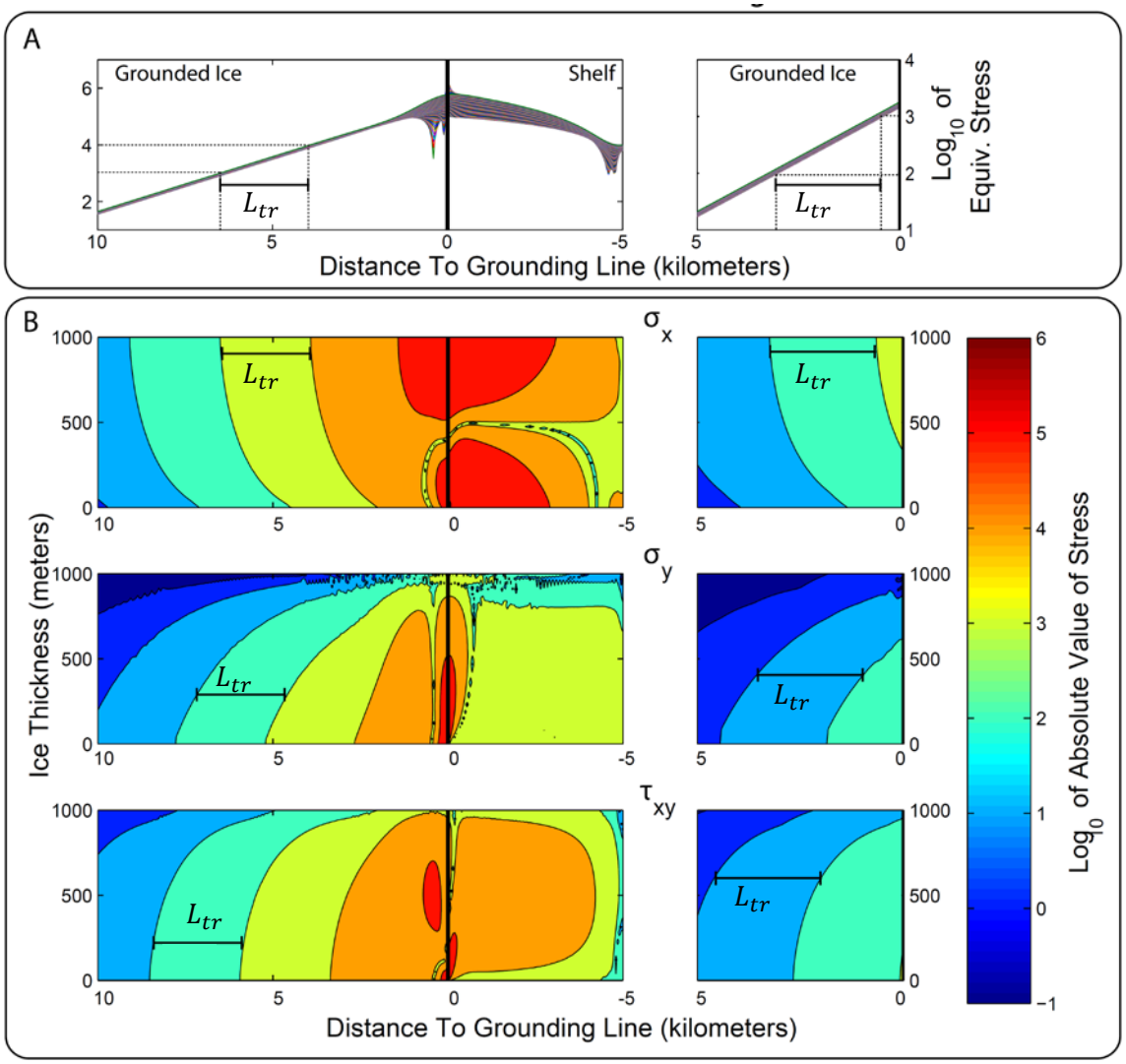

Figure 2.3: Stress distributions for a two-dimensional model with no basal sliding. The panels are the same as in figure 2.2. Stress at the grounding line is higher in the model with an ice shelf than without a shelf, but L_{tr} is the same between the two model setups.

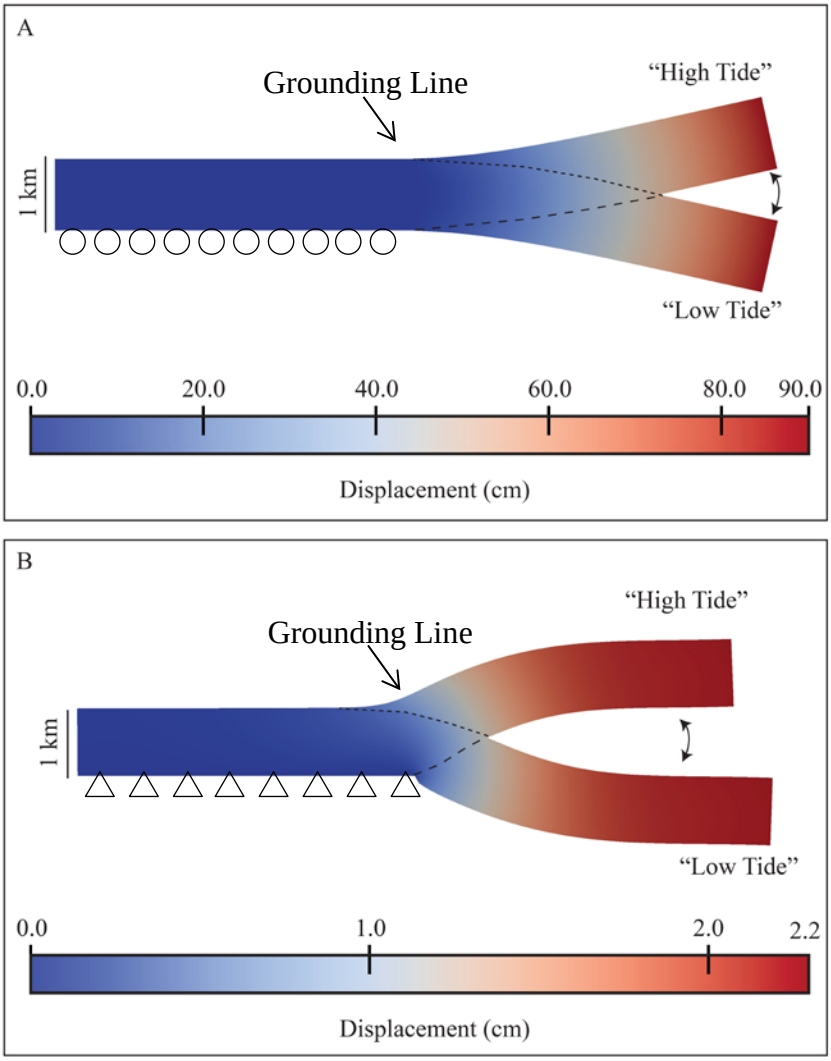

Figure 2.4: Displacement fields for the two-dimensional models with attached shelves. The color shows the overall displacement magnitude, and the mesh is warped by the displacement multiplied, by a factor of 1000 for panel A and by a factor of 50,000 for panel B. Panel A shows the results for the model with a sliding basal condition and panel B shows the results for the model with a fixed basal condition. The high tide position corresponds to a shelf forcing of magnitude $\sigma_{tide} = \rho g \Delta h$ (inward traction) while the low tide position corresponds to a shelf forcing of magnitude of $\sigma_{tide} = -\rho g \Delta h$ (outward traction.

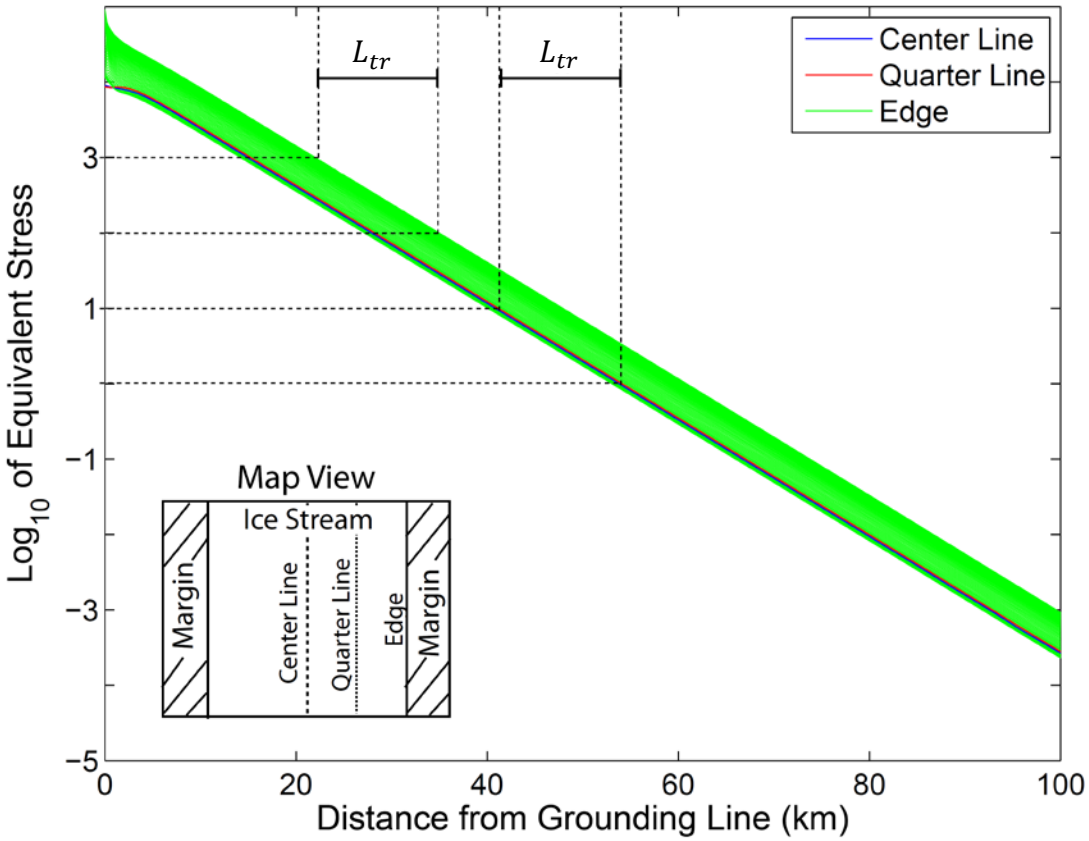

Figure 2.5: Stacked equivalent stress (τ_{eq}) profiles for three different locations in a three-dimensional model with uniform elasticity, a width of 10 kilometers, and a thickness of 1 kilometer. The inset shows the locations of the three profiles in map view. For each location, 101 lines are stacked, taken at 10 meter depth intervals. For the center and quarter lines, there is very little difference in stress value with depth, while for the edge of the ice stream, the stress value changes with depth by about an order of magnitude. However, between all these profiles, L_{tr} is constant.

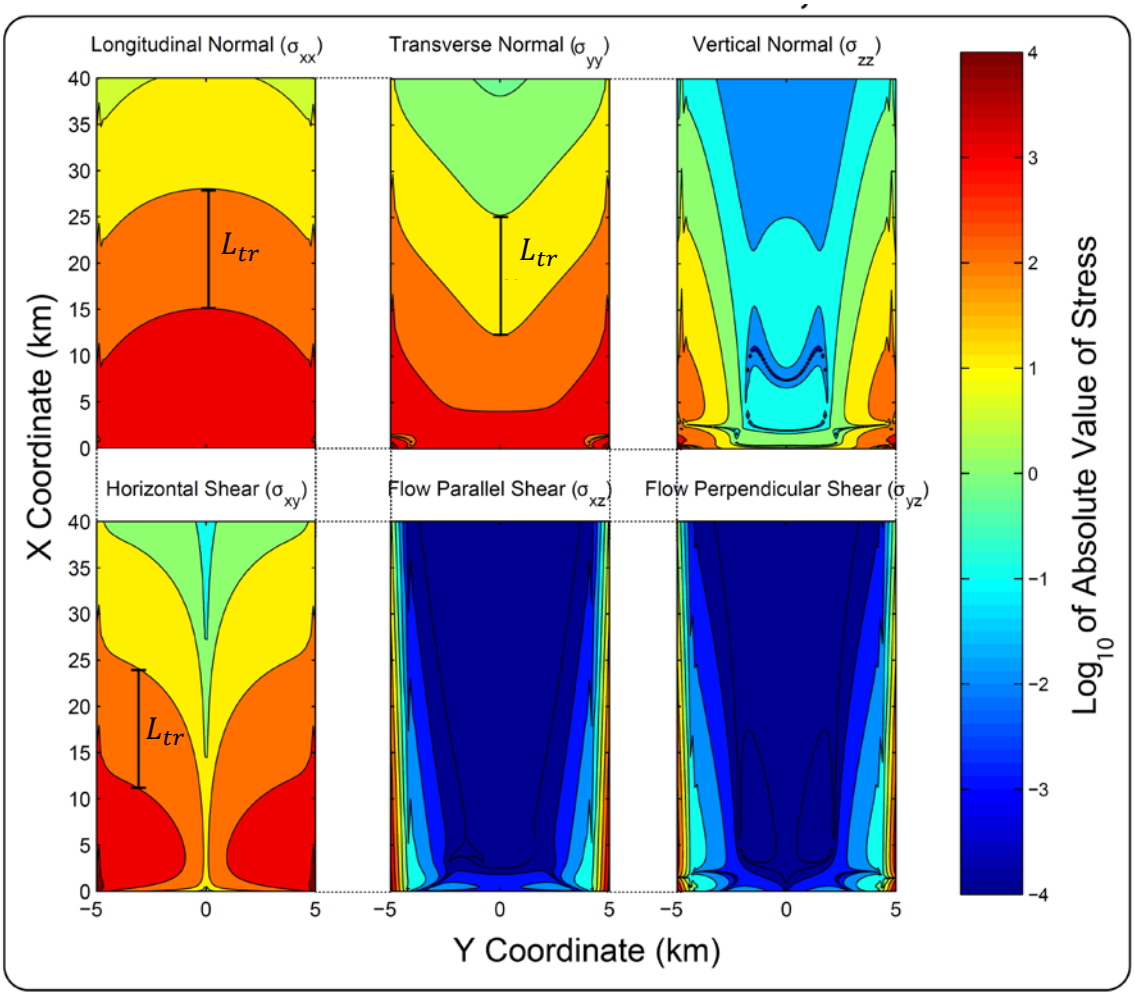

Figure 2.6: Representative stress distribution along the base of a three-dimensional model with homogenous elasticity, showing the six unique stress components. The streaming portion of the model has a width of ten kilometers and a thickness of one kilometer. L_{tr} is drawn in the σ_{xx}, σ_{yy}, and τ_{xy} components where it is easiest to observe.

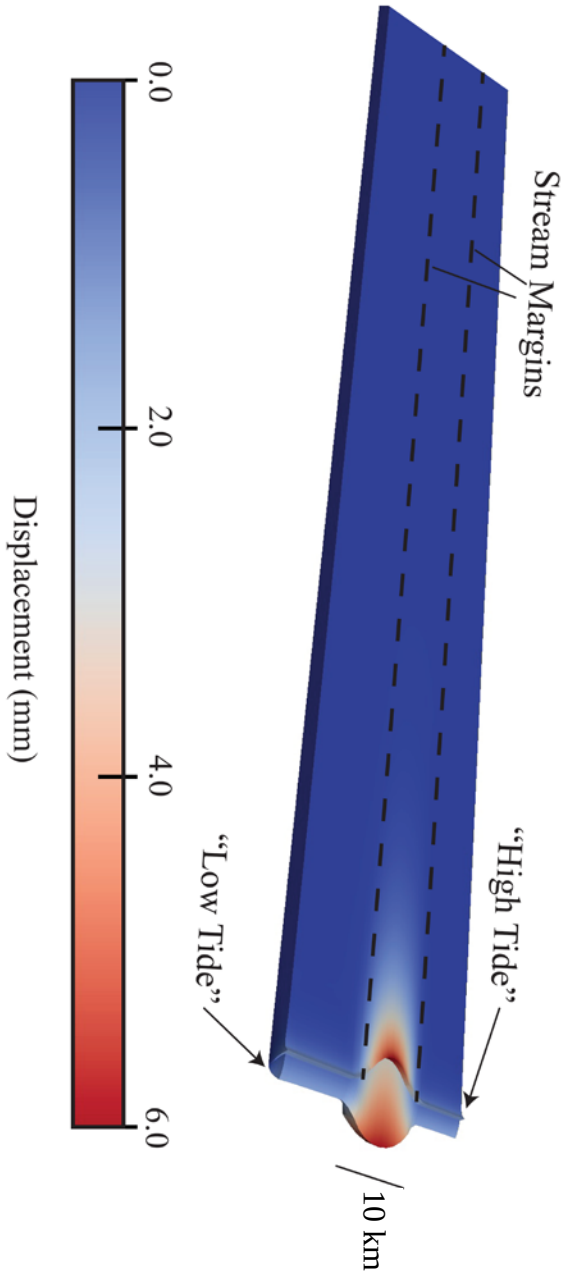

Figure 2.7: Three-dimensional displacement field for a high and a low tidal amplitude. The high tide corresponds to an applied traction of magnitude $\sigma_{tide} = \rho g \Delta h$ and the low tide corresponds to a traction of magnitude of $\sigma_{tide} = -\rho g \Delta h$. The ice stream is 10 kilometers wide, with the surface projection of the lateral margins draw in dashed black lines.

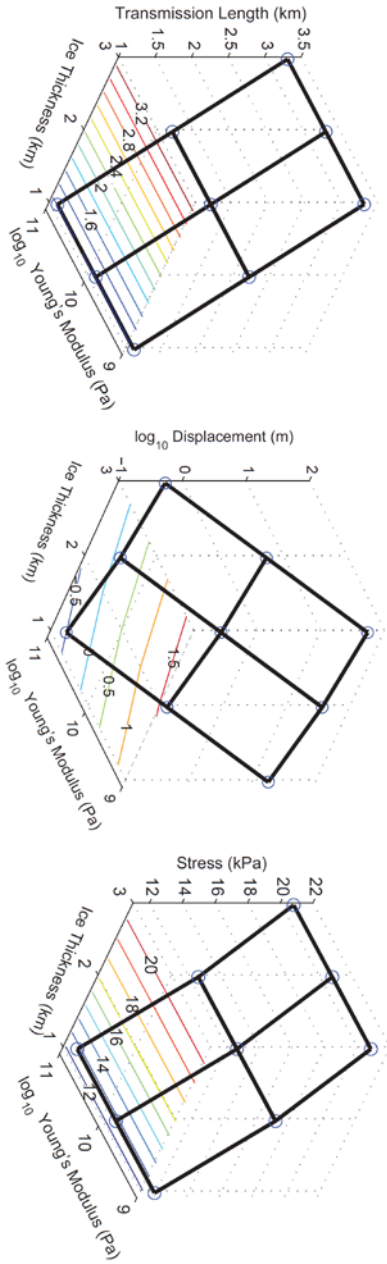

Figure 2.8: Trend in the two-dimensional models as function of Young's modulus (E) and ice thickness (h). The three figures plot the transmission length-scale (L_{tr}), centerline surface displacement above the grounding line, and the centerline equivalent stress at the surface above the grounding line. The circles are the model results, while the colored contours at the bottom of each plot show the values of the quantity on the vertical axis.

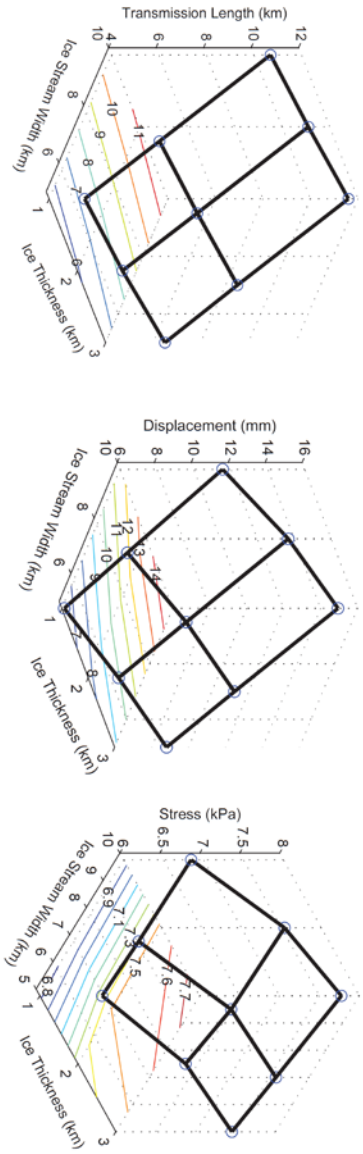

Figure 2.9: Trend in the three-dimensional models as function of ice stream width (*w*) and ice thickness (*h*). The three figures plot the transmission length-scale (L_{tr}), centerline surface displacement above the grounding line, and the centerline equivalent stress at the surface above the grounding line. The circles are the model results, while the colored contours at the bottom of each plot show the values of the quantity on the vertical axis.

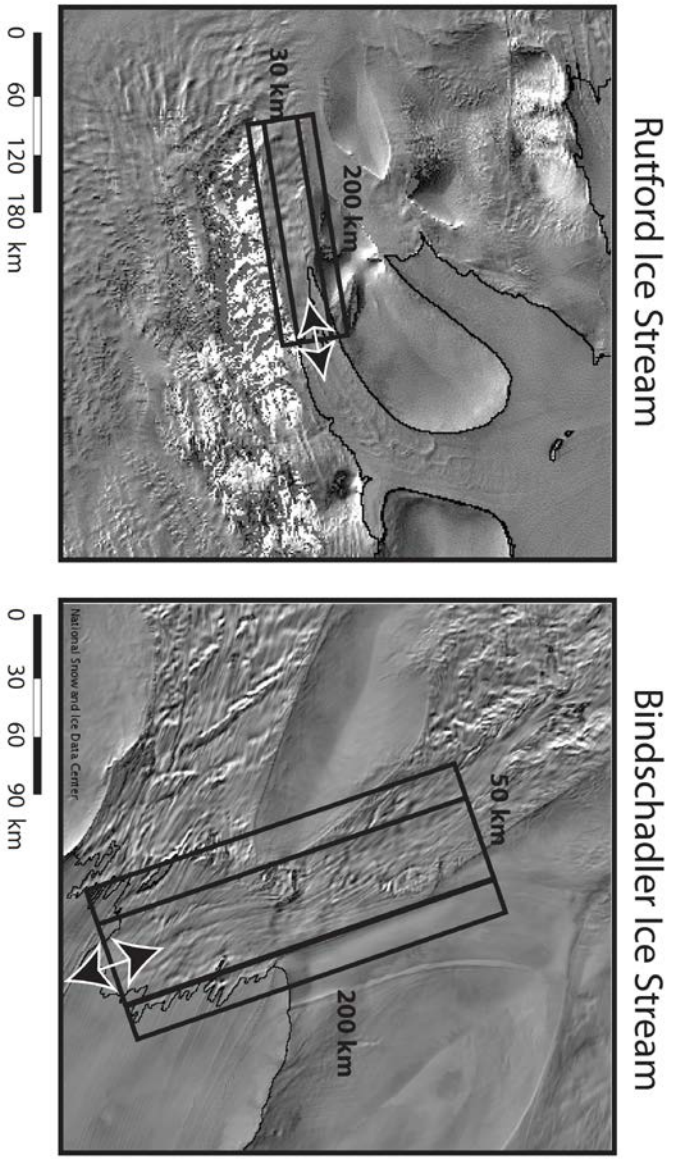

Figure 2.10: Comparison of our side-wall shear models with the real geometry of Rutford Ice Stream, and Bindschadler Ice Stream. The arrow denotes the forced edge, the central region is the sliding portion of the model and the flanking regions are the fixed portions of the model. Numerical values denote the length and width of the modeled ice stream. Background images from the NSIDC RAMP imagery database (`http://nsidc.org/data/ramp/`).

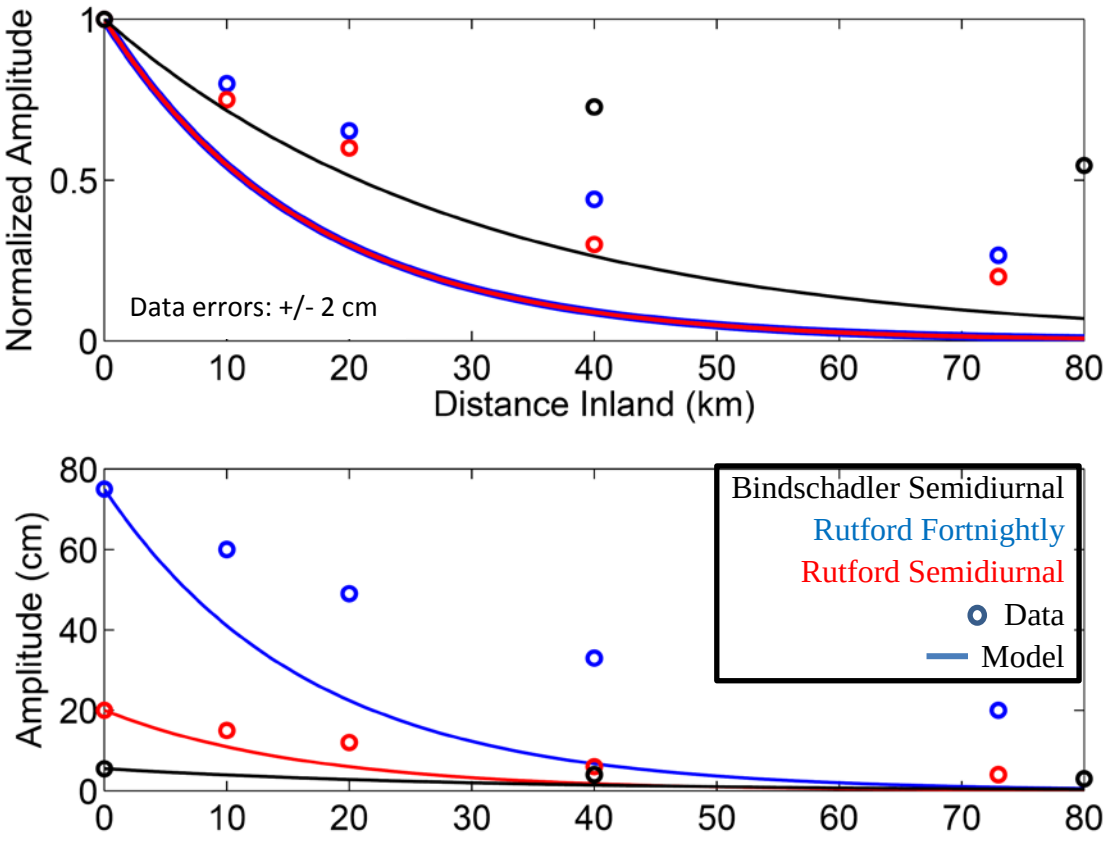

Figure 2.11: Diagram comparing GPS tidal displacement amplitudes to modeled displacement amplitudes. Circles show the data taken from observation on Rutford and Bindschadler Ice Stream (Bindschadler data from figure 2 of Anandakrishnan et al., 2003; Rutford data courtesy of H. Gudmundsson). The error on the approximated tidal displacement amplitudes is two centimeters. The slopes of the modeled surface displacements are taken from models approximating the Rutford Ice Stream and Bindschadler Ice Streams, as shown in table 2.4. As in figure 1.6, the upper panel shows the normalized tidal amplitudes, while the lower panel shows the true amplitude values.

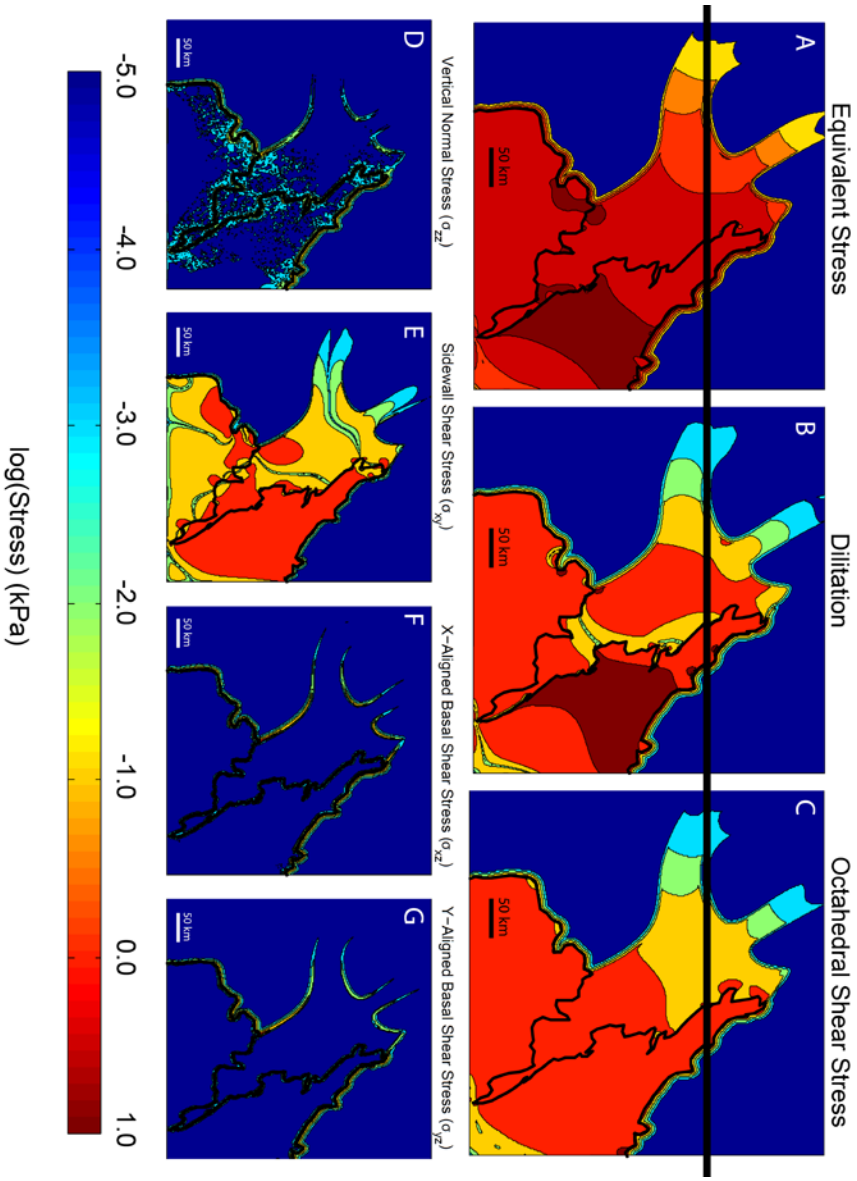

Figure 2.12: Basal stress results from our Whillans Ice Plain model. Panels A-C show equivalent stress, dilatation, and octahedral shear stress, respectively. Panels D-G show vertical normal stress, side-wall shear stress, x-aligned basal shear stress, and y-aligned basal shear stress, respectively. All panels are scaled to the same logarithmic scale, shown at the bottom of the figure. The models are forced only along the grounding line, shown in the panels as the bolded black line.

Parameter	*Symbol*	*Value*
Young's Modulus	E	9.33 GPa
+Poisson's Ratio	ν	0.325
*Shear Modulus	G	3.52 GPa
*Bulk Modulus	K	8.90 GPa
+Density (at 0 °C)	ρ	917 kg/m^3
+Viscosity coefficient	A	5.86x10^{-6} MPa^3/s
+Stress exponent	n	3

Table 2.1: Elastic and viscous parameters used to define the ice properties in our finite element modeling. Values of elastic parameters, except for density, are taken from Petrenko and Whitford (2002) using data from Gammon et al. (1983A; 1983B). Viscous parameters are taken from Pateron (1997). Parameters marked with an asterisk (*) denote quantities that are calculated from the other moduli and material properties. Parameters marked with a plus (+) are fixed through all models.

Fixed Base				*Sliding Base*			
Condition	*Component*	L_{tr} *(km)*	*St. Dev.*	*Condition*	*Comp.*	L_{tr} *(km)*	*St. Dev.*
Shelf	X	2.586	0.004	Shelf	X	1.304	9.049*
	Y	2.619	0.095		Y	1.101	0.013
	XY	2.590	0.015		XY	1.078	1.4e-5
Axial Only	X	2.517	0.023	Axial Only	X	∞	N/A
	Y	2.618	0.068		Y	N/A	N/A
	XY	2.616	0.018		XY	N/A	N/A

Table 2.2: Transmission length-scales (L_{tr}) for the two-dimensional models shown in figures 3 and 4. See text for description of how the parameters are found. All cases save the marked (*) case have very low standard deviations. In the marked case, the standard deviation is large as the value of σ_x falls to zero near the middle of the ice stream vertically, making L_{tr}vary dramatically near these locations. Near the upper and lower portions of the ice stream, the stress decay for σ_x is more consistent with the values for the other stress components.

Model #	*Figure #*	*h (km)*	*E (GPa)*	*Disp. @ GL (mm)*	*Stress @ GL (kPa)*	L_{tr} *(km)*
1	2.3	1	9.33	1.68	11.80	2.5
2	2C.1	2	9.33	3.46	17.06	5.1
3	2C.2	3	9.33	5.22	20.75	7.6
4	2C.3	1	0.933	16.83	11.80	2.5
5	2C.4	2	0.933	34.59	17.06	5.1
6	2C.5	3	0.933	52.24	20.75	7.6
7	2C.6	1	93.3	0.17	11.80	2.5
8	2C.7	2	93.3	0.35	17.06	5.1
9	2C.8	3	93.3	0.52	20.75	7.6

Table 2.3: Model parameters and results from our two-dimensional models. The displacement measurement is the magnitude of the modeled surface displacement vector above the grounding line (i.e., at *x=0*). The stress value is the equivalent stress at the surface above the grounding line. The transmission length-scale L_{tr} is the value found for the decay of the equivalent stress, which matches the value found using the surface displacement magnitude.

Model #	*Figure #*	*h (km)*	*w (km)*	*E (GPa)*	*Disp. @ GL (mm)*	*Stress @ GL (kPa)*	L_{tr} *(km)*
1	2.6	1	10	9.33	6.13	6.779	12.2
2	2D.1	2	10	9.33	7.64	7.349	12.7
3	2D.2	3	10	9.33	8.81	7.453	12.7
4	2D.3	1	14	9.33	8.29	6.817	13.6
5	2D.4	2	14	9.33	10.04	7.500	15.0
6	2D.5	3	14	9.33	11.22	7.585	17.5
7	2D.6	1	20	9.33	11.55	6.845	18.4
8	2D.7	2	20	9.33	13.68	7.439	19.6
9	2D.8	3	20	9.33	14.94	7.775	24.6
10	2D.9	1	10	0.933	61.30	6.790	25.6
11	2D.10	1	10	93.3	0.61	4.778	26.7
12*	2D.11	2	50	9.33	31.99	7.584	69.1
13	2D.12	2	40	9.33	25.85	7.581	52.2
14**	2D.13	2	30	9.33	19.75	7.577	38.2

Table 2.4: Model parameters and results from our two-dimensional models. The stress, displacement, and transmission length-scales are found in the same manner as discussed in the description of table 2.3.

Appendix 2A: Importance of the Ice Shelf

As all of the ice streams that display far-field tidal effects have a connected ice shelf, we now consider the role that the ice shelf plays as the intermediary between the ocean tides and the grounded ice stream. Recall the two-dimensional model results shown in figures 2.2 and 2.3 for models both with and without an ice shelf. For a given basal condition, any variation between the two model results must be due to the presence of the shelf alone.

For the model with a frozen base, the presence of an ice shelf has two effects. First, there is a perturbation to the stress field near the grounding line (about two kilometers inland at most), due to flexural stresses introduced by the ice shelf. Second, the overall magnitude of stresses in the ice stream is elevated compared to models with only axial loading as there is an overall increase in the magnitude of the loading applied in the model. This effect does not change L_{tr}. Thus for ice with no basal sliding, including an ice shelf affects the magnitude, but not the nature of the stress field, far inland of the grounding line.

For the two-dimensional model with basal sliding, stresses due to ice flexure decay to inconsequential levels 5-7 kilometers inland of the grounding line. Beyond this point, the stress state of the ice stream is identical to the stress state for a model with axial loading only. Thus, for an ice stream with no basal resistance, the ice shelf does not influence the modeled results farther inland than the first five to ten kilometers of grounded ice.

The general finding that flexural stresses only perturb the stress field near the grounding line is consistent with the observations of ice flexure transmission of ten

kilometers or less, as summarized in table 1.1. Additionally, our constant loading shelf condition overestimates flexural stress by almost a factor of four compared to a more realistic floating condition (see appendix 2B). This indicates that flexural stresses may decay to small values over a shorter distance than predicted here. Our models reproduce the observation that the flexural stresses, as induced by the presence of an ice shelf, are not important far inland of the grounding line.

The basal condition beneath the ice stream determines the influence of the ice shelf on the overall magnitude of the stress in the far-field ice stream. As ice streams have little basal resistance, the finding that the overall stress magnitude is independent of the ice shelf outside of the flexure zone is applicable here. Our interest is in the value of stresses many tens of kilometers inland of the grounding line, thus we can safely neglect the ice shelf in our models without changing the transmission of tidal, non-flexural stresses.

Appendix 2B: Flotation Condition for a One-Dimensional Ice Shelf

As shown in figure 2.1, we apply two tractions to a model ice shelf to simulate the stress change on an ice shelf due to a change in tide height. First, we consider the axial load of the tide on the ice shelf's edge. A simple comparison is to look at the stress within an axial bar that is compressed axially with a constant stress. Assume the bar to be fixed at the unforced end. By the compatibility condition:

$$\delta\sigma/_{\delta x} = 0 \tag{2.B1}$$

the stress and strain in such a model must be constant throughout the bar. This corresponds to infinite stress-transmission.

Second, we model the ice shelf as a Bernoulli-Euler beam subjected to a distributed load, with this load coupled to the beam deflection by a flotation condition. This approach is similar to the methodology of Reeh et al. (2000). The governing equation of such a model is:

$$EI\frac{\delta^4 w}{\delta x^4} = \rho_w g(\Delta h - w) \tag{2.B2}$$

where ρ_w is the density of water, g is gravitational acceleration, w is the (vertical) deflection of the beam, E is the Young's modulus of ice, $I = \left(\frac{w}{12}\right) \cdot (h)^3$ is the second moment of area for the ice shelf.

The solutions of this equation for multiple ice shelf lengths are found and shown in figure 2.B1. The primary result is that, for a one meter tide, a shelf of longer than five kilometers no longer influences the stresses at the grounding line, meaning that for our

purposes, we only need to consider a shelf of five kilometers length in our finite element modeling.

Additionally, we model a linearly thinning ice shelf (through the modification of *I*, using $I = \left(\frac{w}{12}\right) \cdot \left([h_0 - (h_0 - h_1)]\frac{x}{L}\right)^3$ where the thickness linearly changes from h_0 to h_1) and find that this has only a small influence on the stress and deflection throughout the shelf. Thus these effects will not be considered further.

Lastly, we model the results for a simpler, uncoupled stressing condition. In figure 2.B1, the red dashed line corresponds to a constant loading function equal to $\rho_w g \Delta h$. This simpler condition overestimates the stress and deflection over the model domain compared to the more correct flotation condition. However, as the boundary condition does not depend on, and thus is decoupled from, the deflection *w*, we use this constant loading as our ice shelf boundary "pseudo-flotation" condition in our finite modeling.

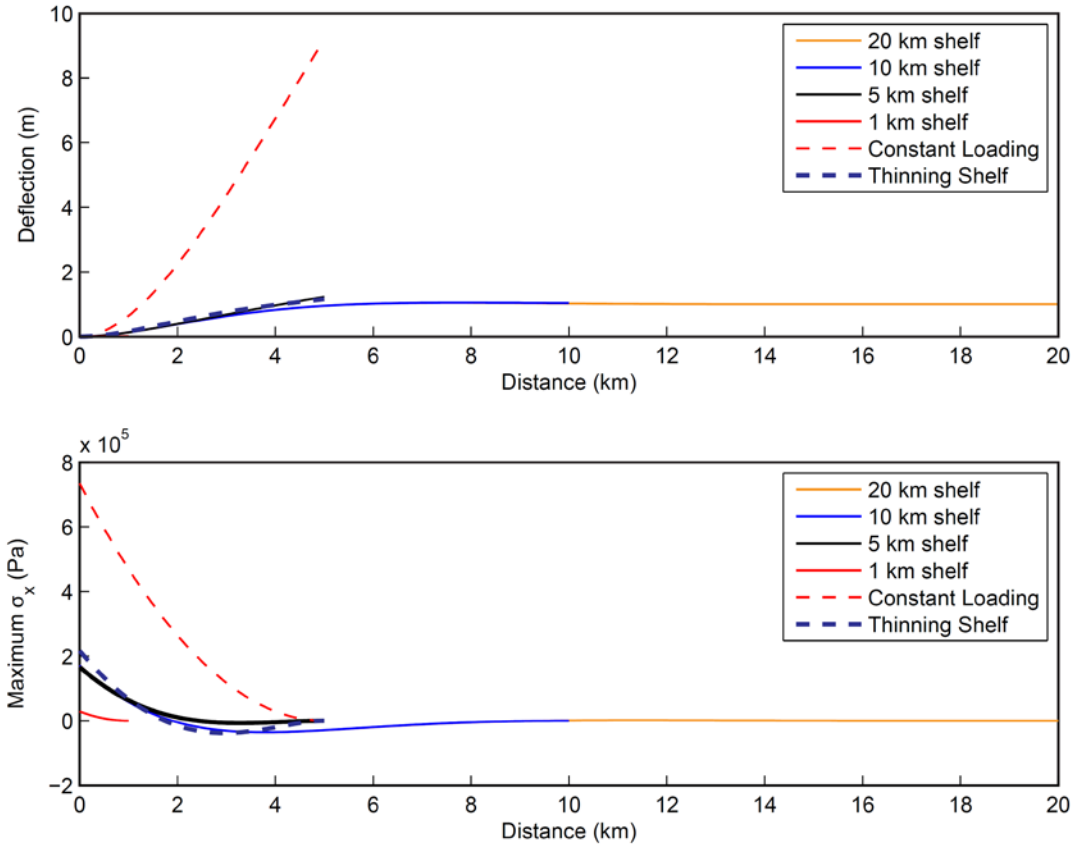

Figure 2B1: Results of the one-dimensional flexural beam approximation of a floating ice shelf. The upper figure shows the beam deflection while the lower section shows the stress at the upper edge of the beam. See text for a description of the governing equations and boundary conditions for the models shown.

Appendix 2C: Two-Dimensional Model Results

Here, we present the complete summary of our model results for our "frozen bed" model, as demonstrated in figure 2.3. We ran a total of nine models, investigating the dependence of the stress and displacement distributions on the ice thickness, *h*, and the ice's elastic modulus, *E*. Table 2.3 provides details to each model, including the values of *h* and *E*, as well as the values of basal stress and surface displacement at the grounding line (i.e., the maximum values), and the e-folding length of the stress and displacement decay. Figures 2C.1 to 2C.8 demonstrate the stress and displacement distributions in each model not shown in the main paper, following the example set by figure 2.3.

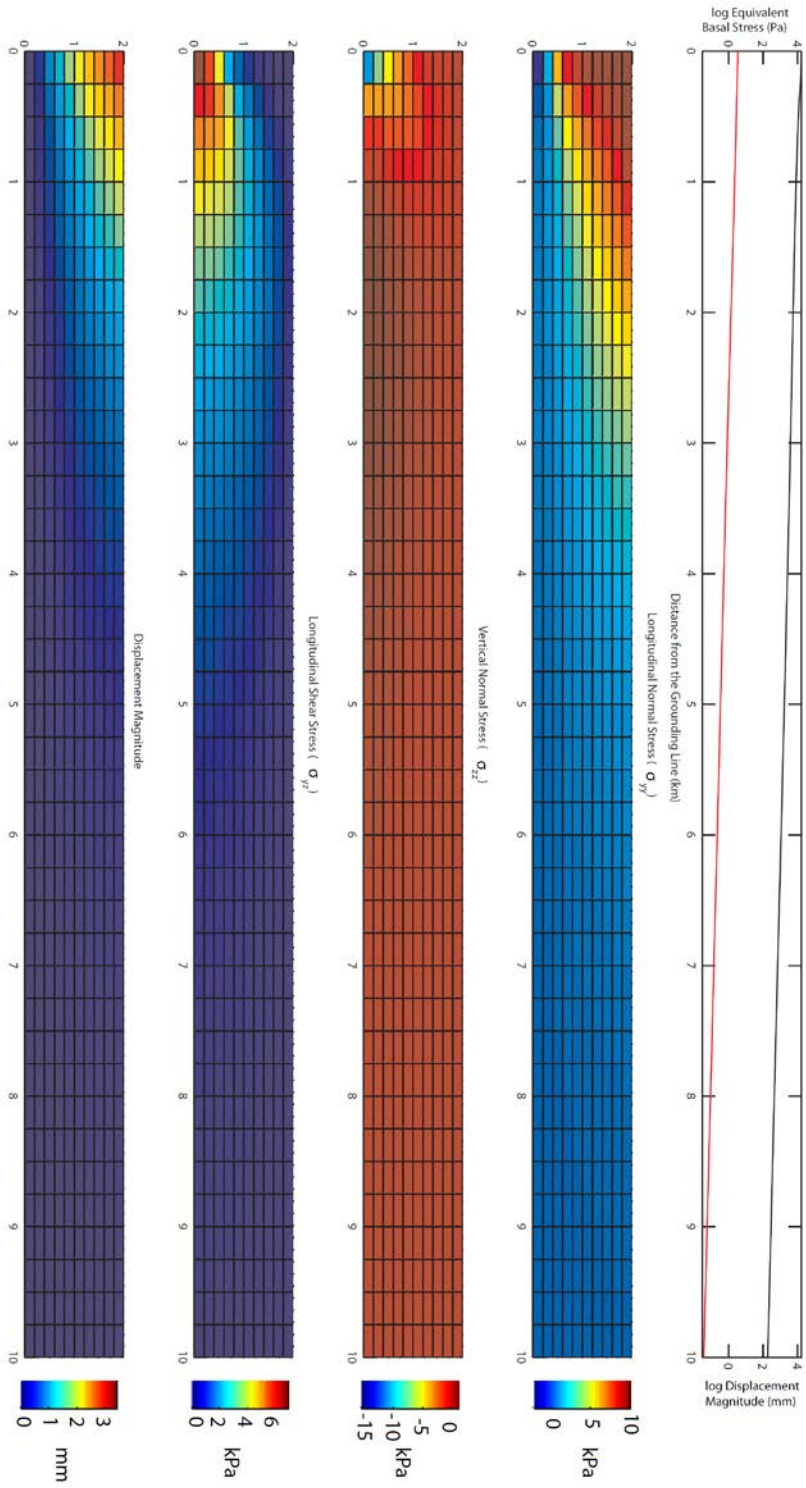

Figure 2C.1: Stress and displacement fields for the two-dimensional frozen bed model with *h=2 km* and *E=9.33 GPa.*

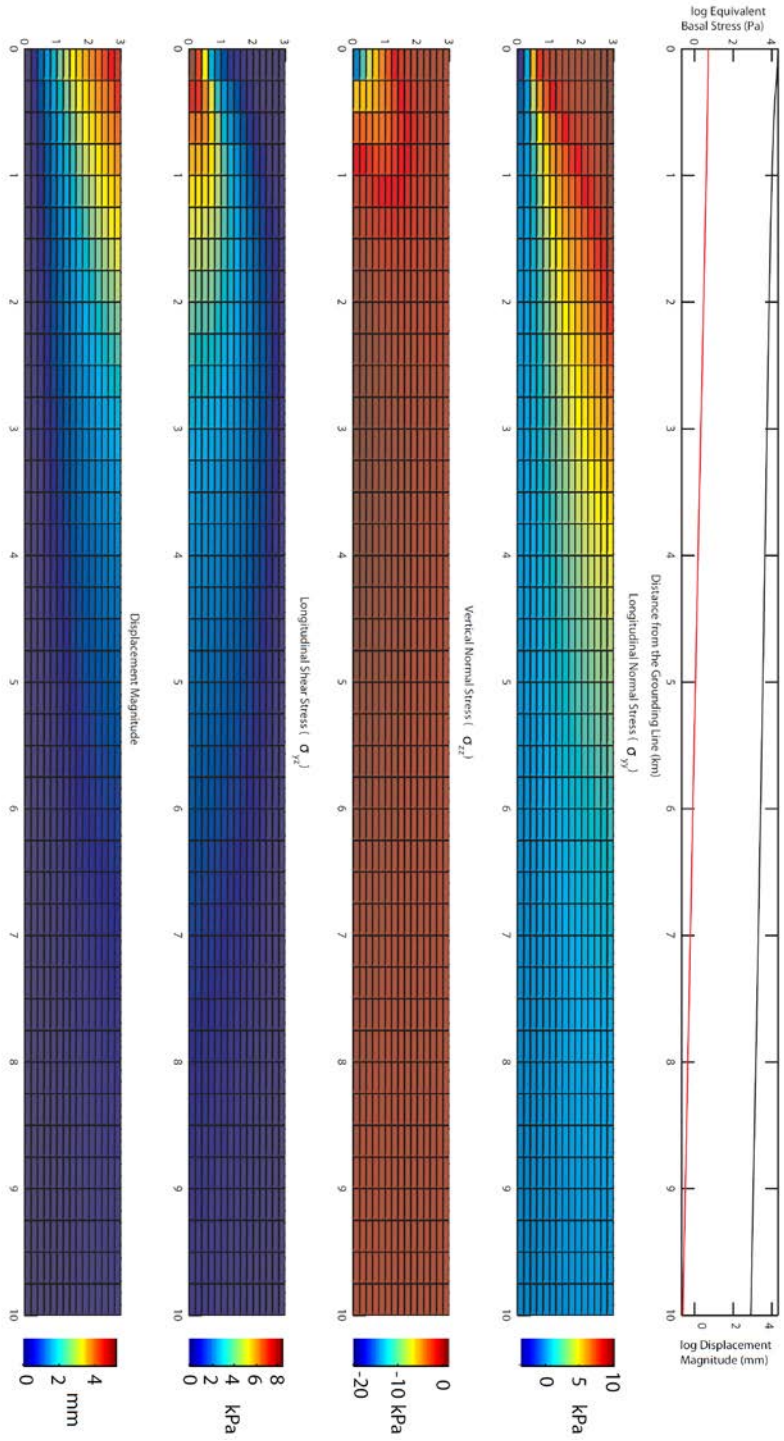

Figure 2C.2: Stress and displacement fields for the two-dimensional frozen bed model with *h=3km* and *E=9.33 GPa.*

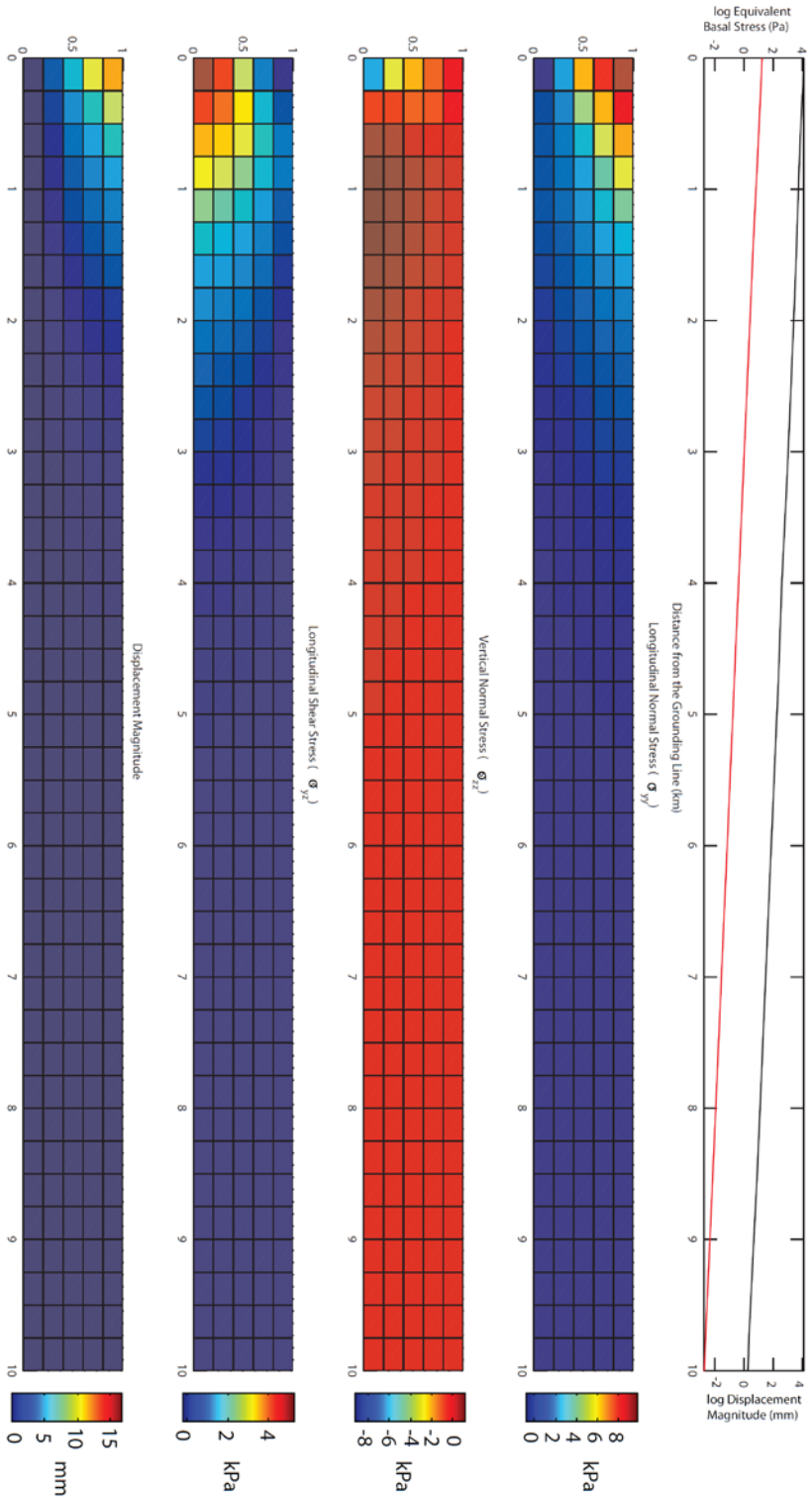

Figure 2C.3: Stress and displacement fields for the two-dimensional frozen bed model with *h=1km* and *E=0.933 GPa.*

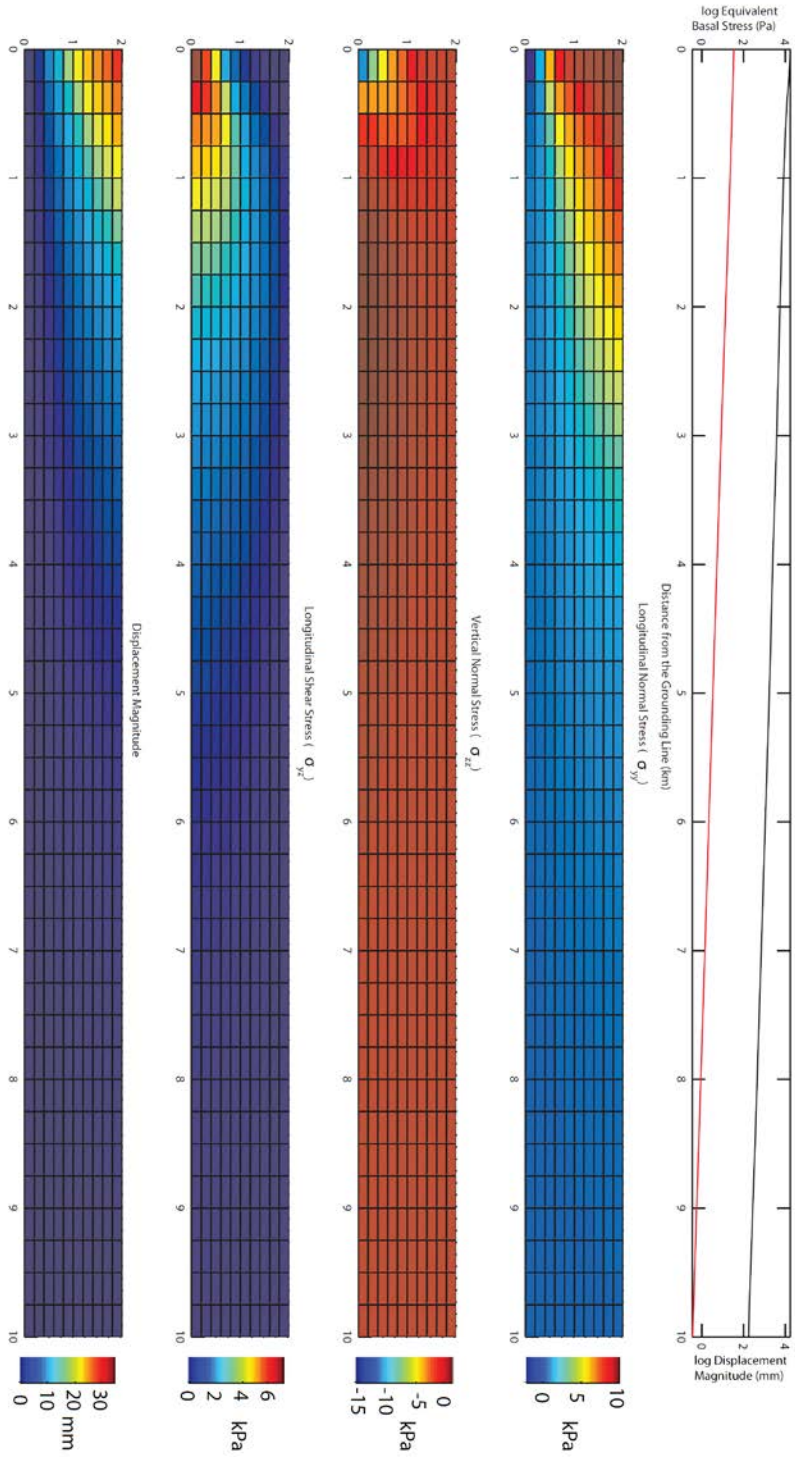

Figure 2C.4: Stress and displacement fields for the two-dimensional frozen bed model with *h=2km* and *E=0.933 GPa.*

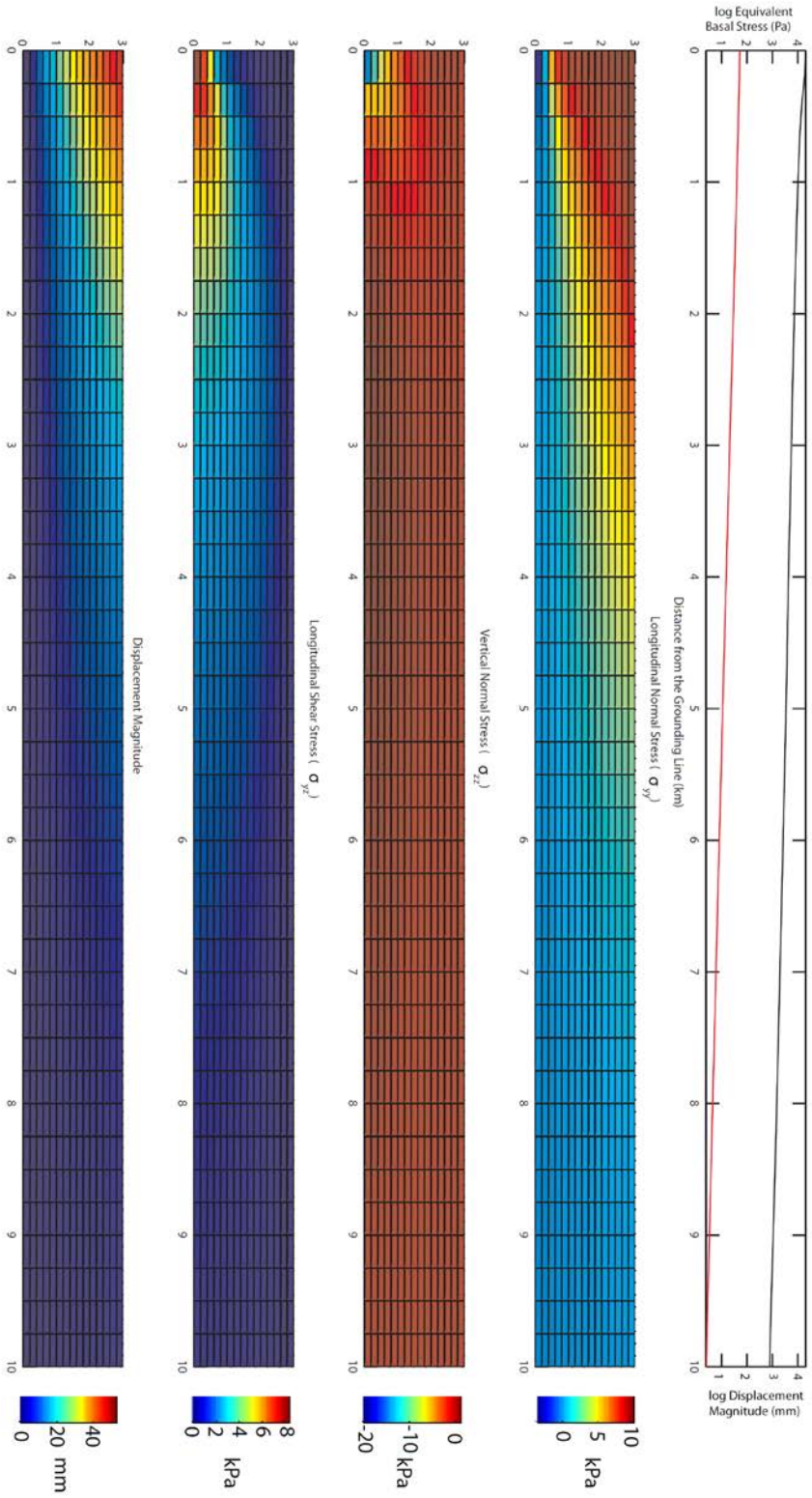

Figure 2C.5: Stress and displacement fields for the two-dimensional frozen bed model with *h=3km* and *E=0.933 GPa.*

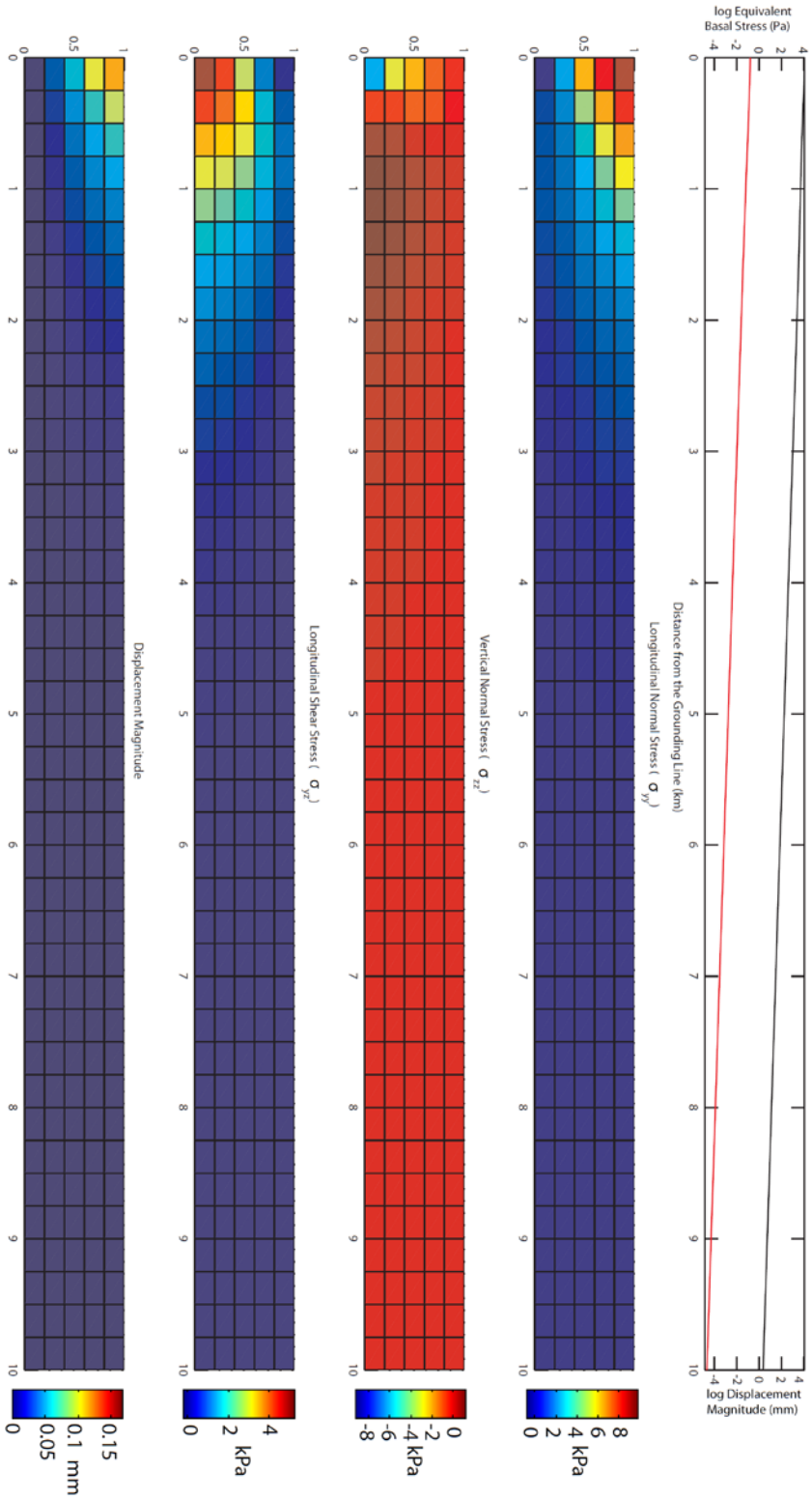

Figure 2C.6: Stress and displacement fields for the two-dimensional frozen bed model with *h=1km* and *E=93.3 GPa.*

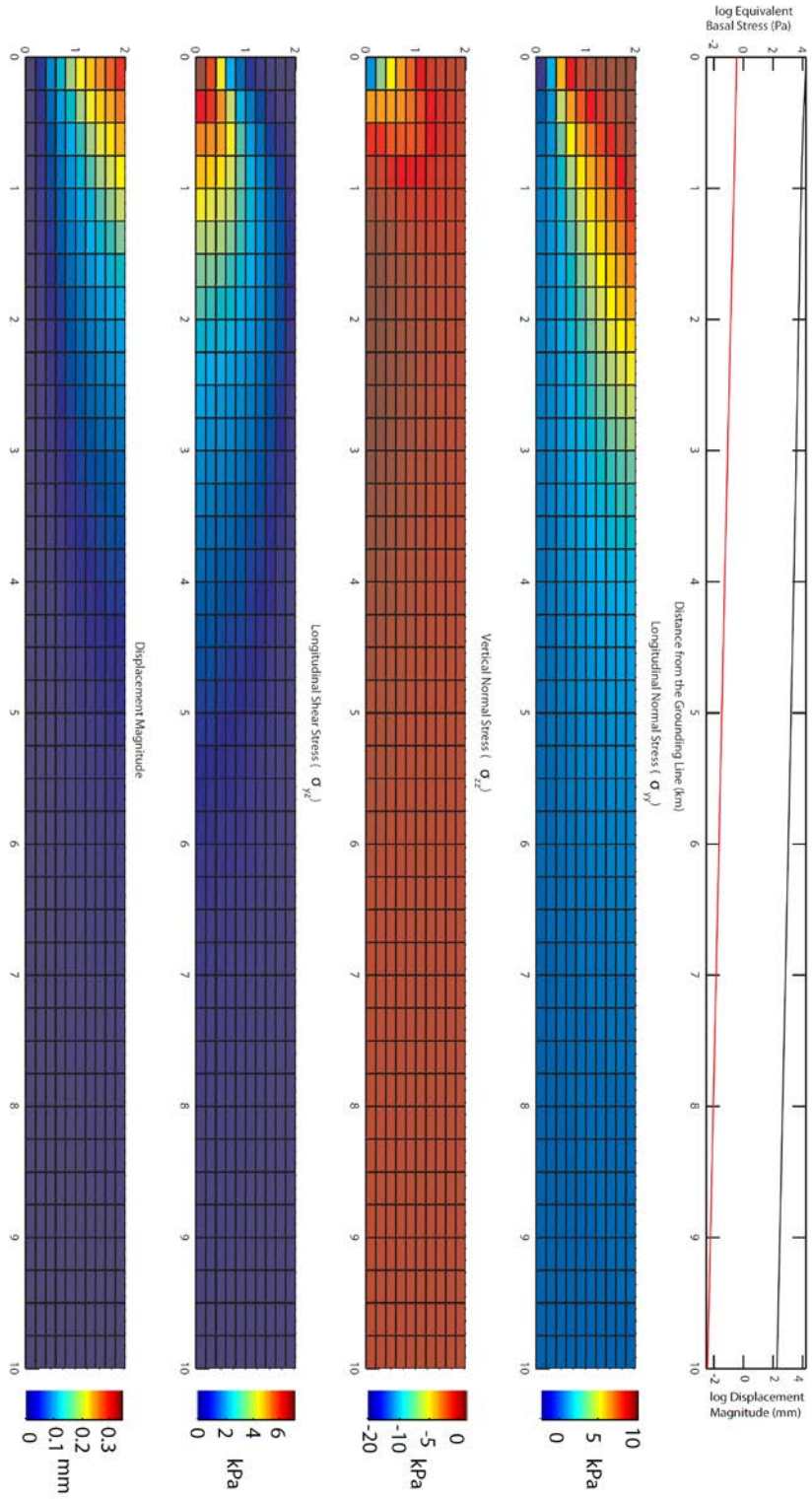

Figure 2C.7: Stress and displacement fields for the two-dimensional frozen bed model with *h=2km* and *E=93.3 GPa.*

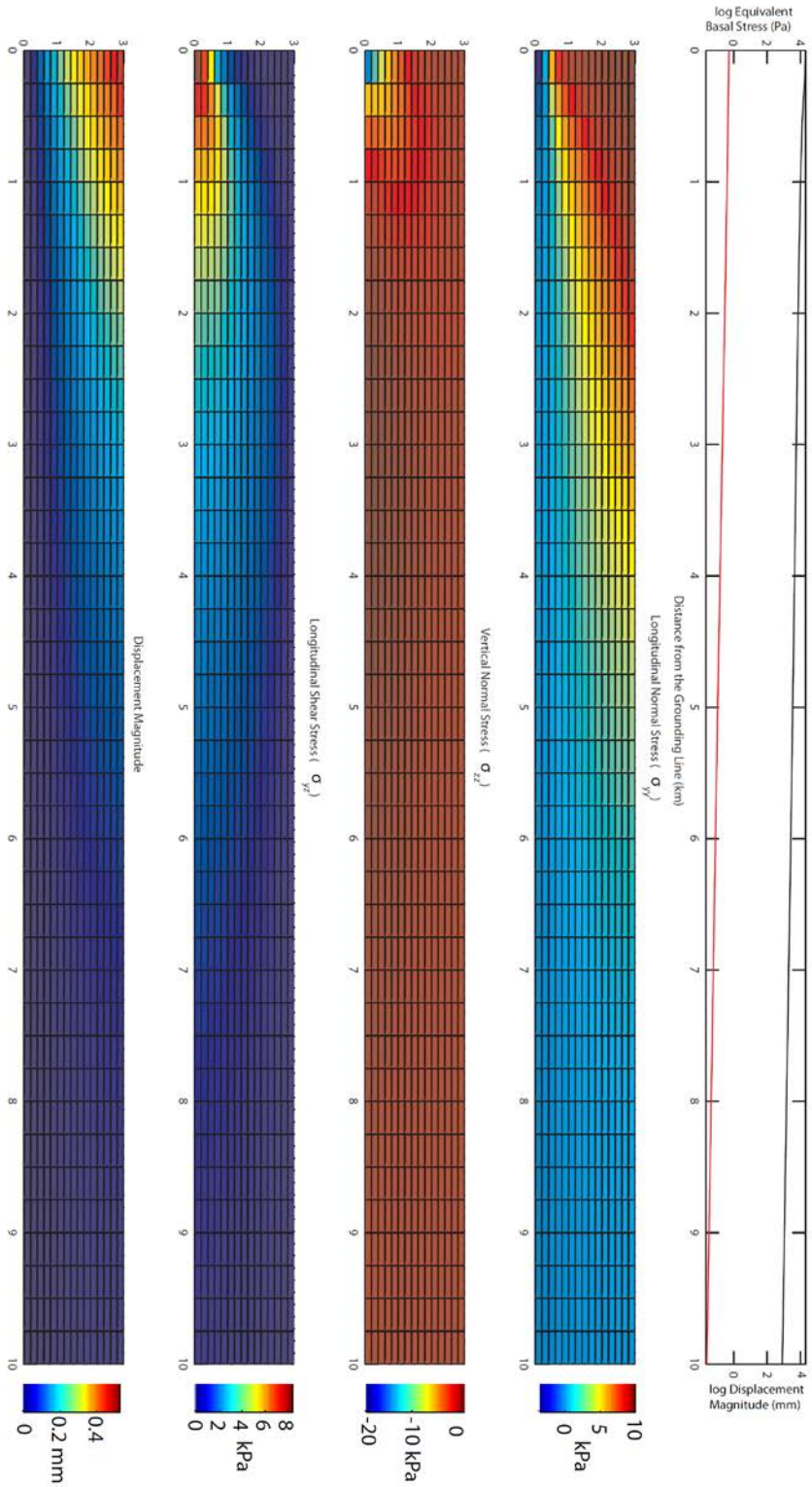

Figure 2C.8: Stress and displacement fields for the two-dimensional frozen bed model with *h=3km* and *E=93.3 GPa.*

Appendix 2D: Three-Dimensional Model Results

In this section, we present the results from our entire three-dimensional model suite. In these models, we varied the ice thickness, *h*, the ice stream width, *w*, and the elastic modulus *E*. We present a total of 14 model results. The first nine models (figures 2.6 and figures 2D.1 to 2D.8) explore the dependence of the results on the geometric parameters *h* and *w*. Models 10 and 11 (figures 2D.9 and 2D.10) demonstrate the linear dependence of the model results on the elastic modulus. Models 12 to 14 (figures 2D.11 to 2D.13) represent the geometries of Bindschadler Ice Stream, Pine Island Glacier, and Rutford Ice Stream, respectively. Due to the lack of GPS data from Pine Island Glacier, these model results are not compared to observations. Table 2.4 summarizes the model parameters, as well as the output results of surface displacement and basal stress at the grounding line in the middle of the ice stream (the global maximum value), as well as the e-folding length in each model. Figures 2D.1 to 2D.13 show the modeled stress distributions, following the example of figure 2.6 from the main body of this paper.

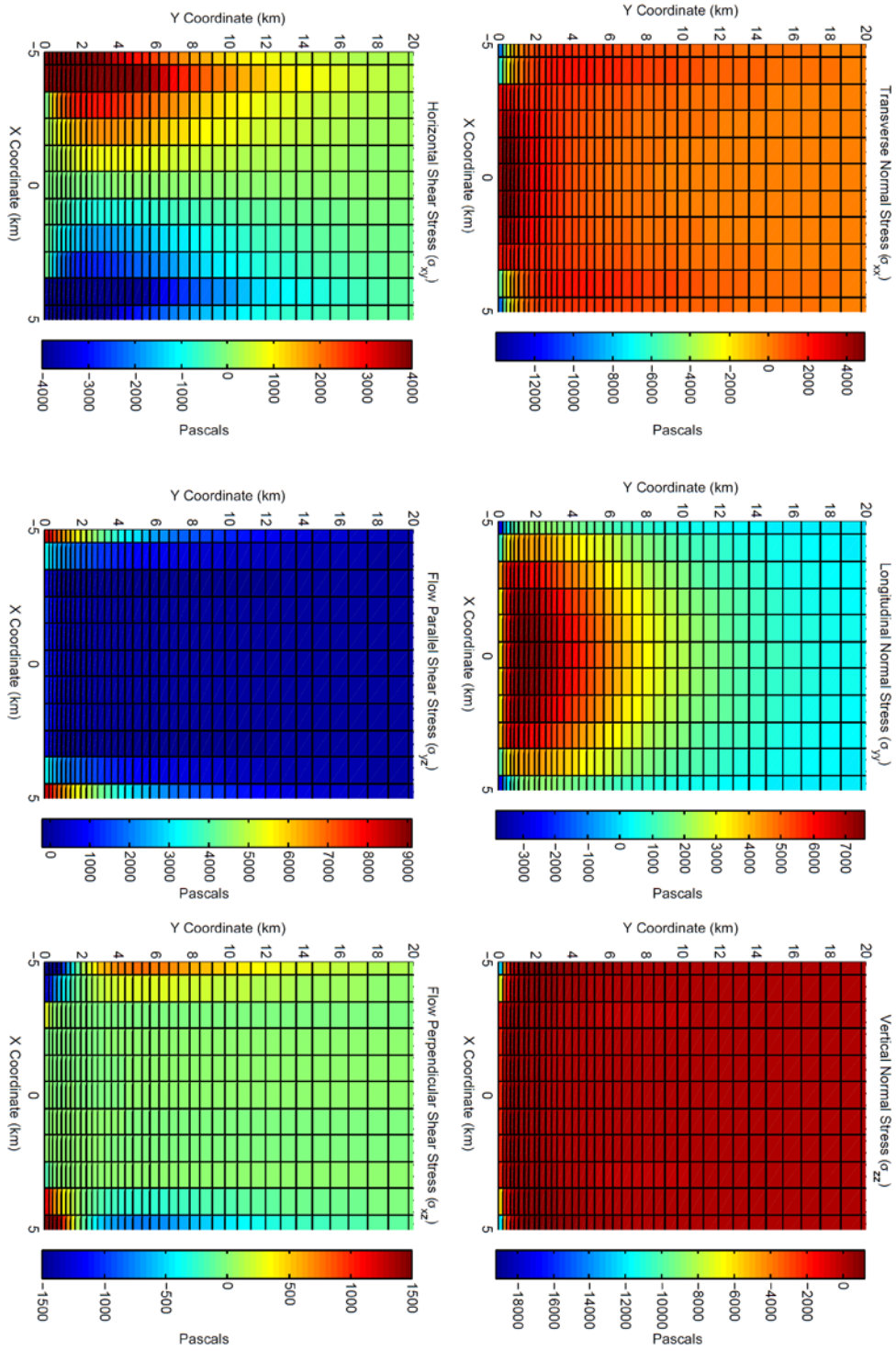

Figure 2D.1: Stress field for the three-dimensional model with *h=2 km, w=10 km,* and *E=9.33 GPa*.

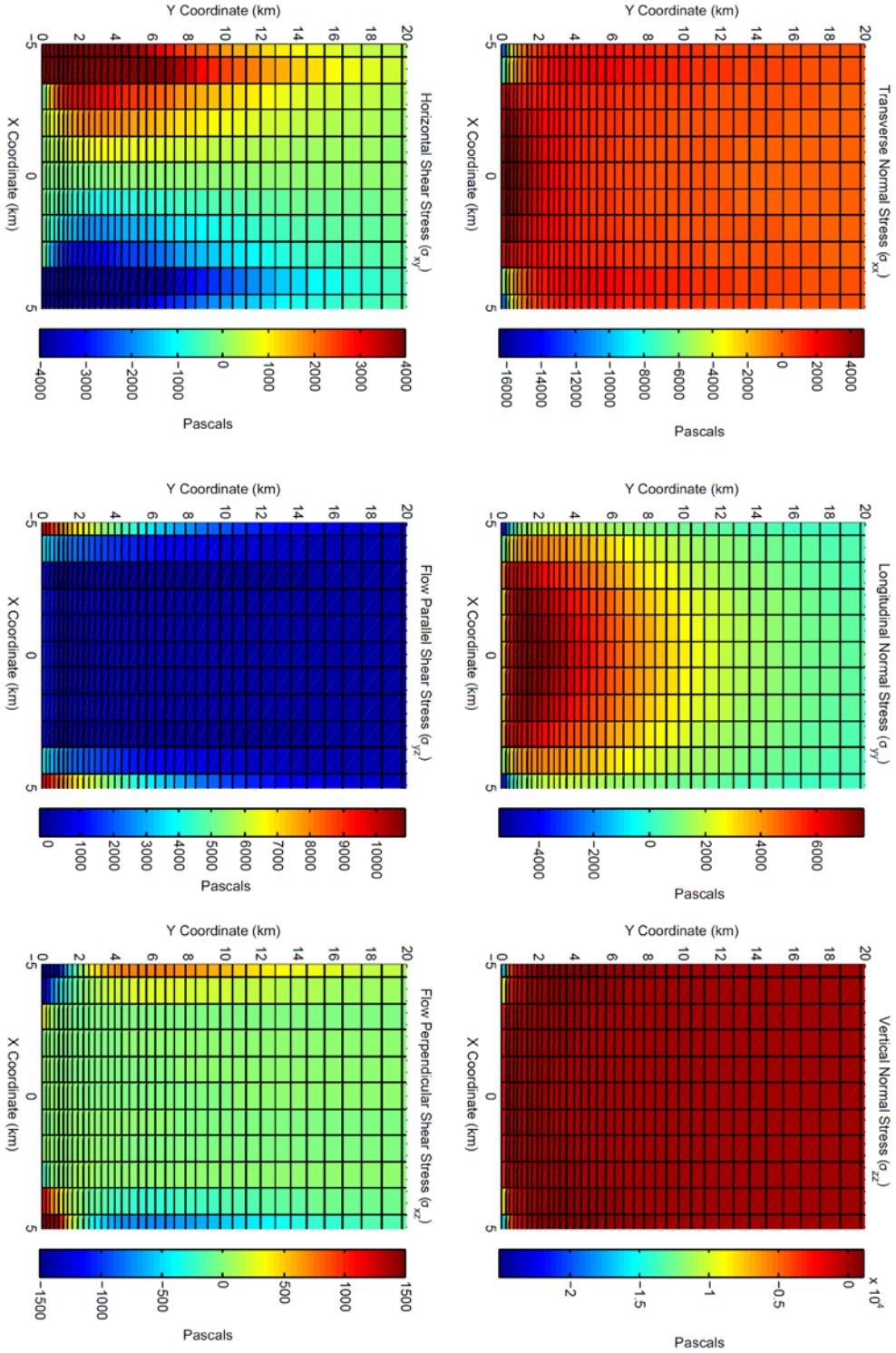

Figure 2D.2: Stress field for the three-dimensional model with *h=3 km, w=10 km,* and *E=9.33 GPa.*

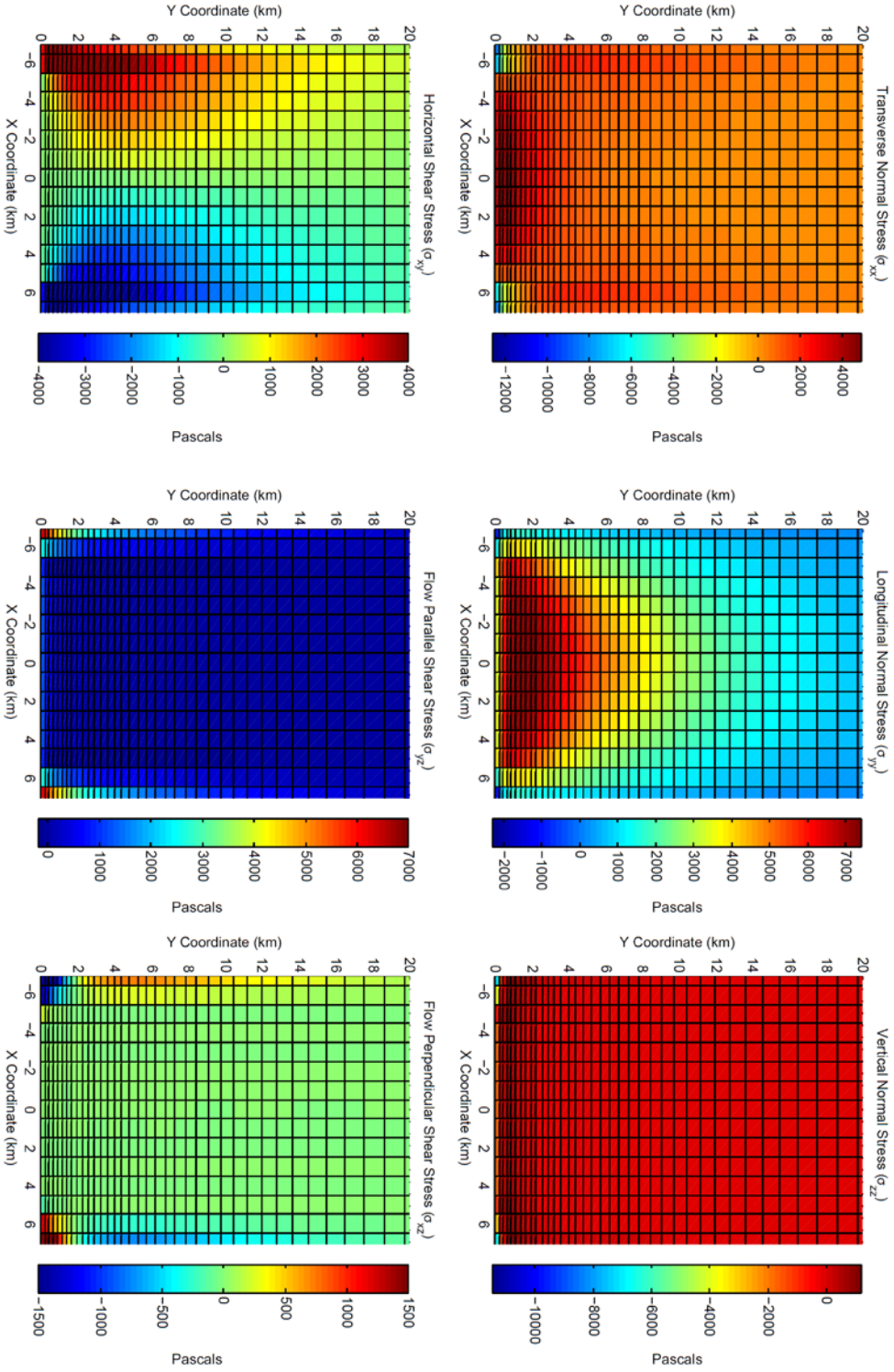

Figure 2D.3: Stress field for the three-dimensional model with *h=1 km, w=14 km,* and *E=9.33 GPa*.

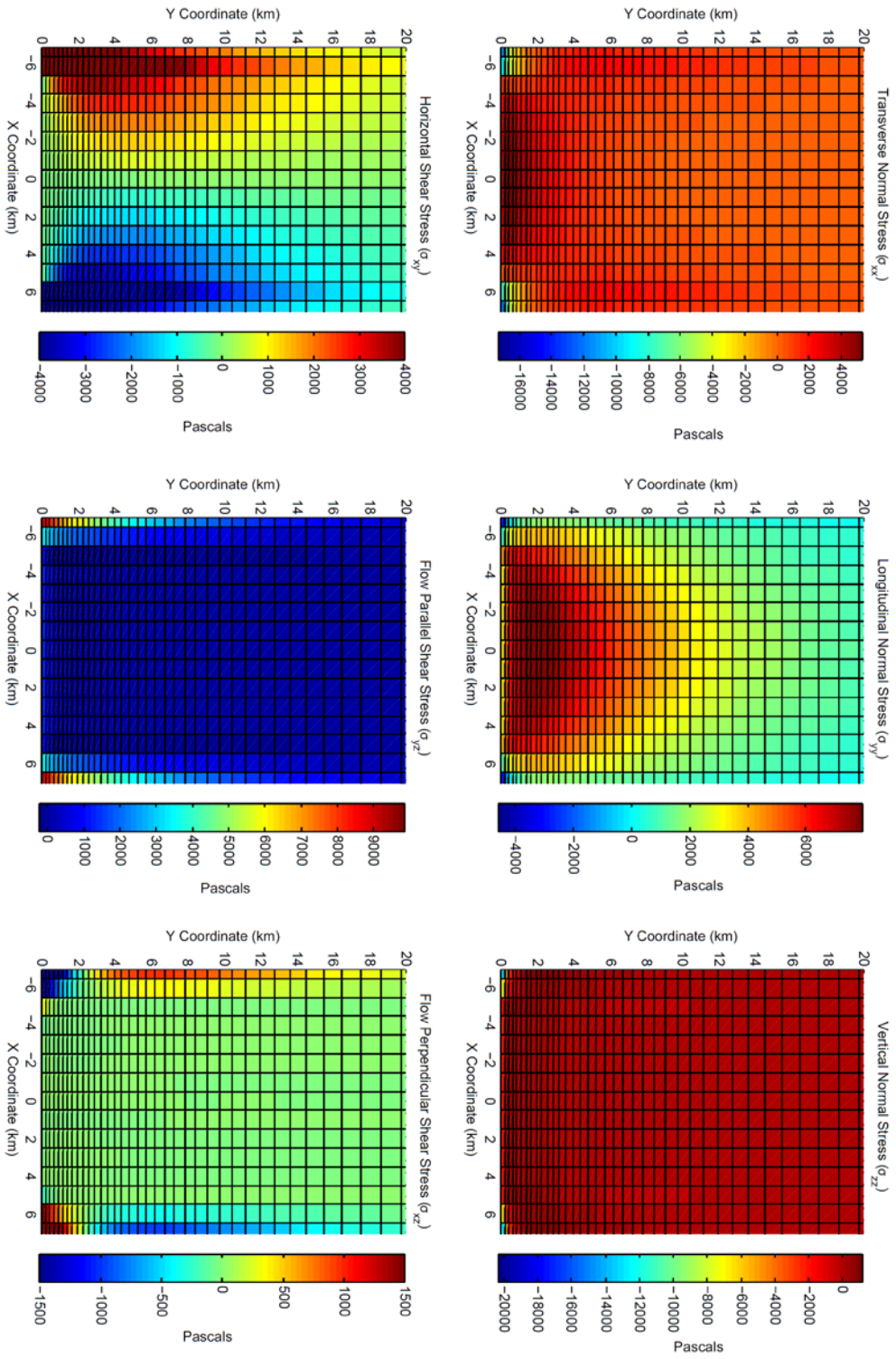

Figure 2D.4: Stress field for the three-dimensional model with *h=2 km, w=14 km,* and *E=9.33 GPa*.

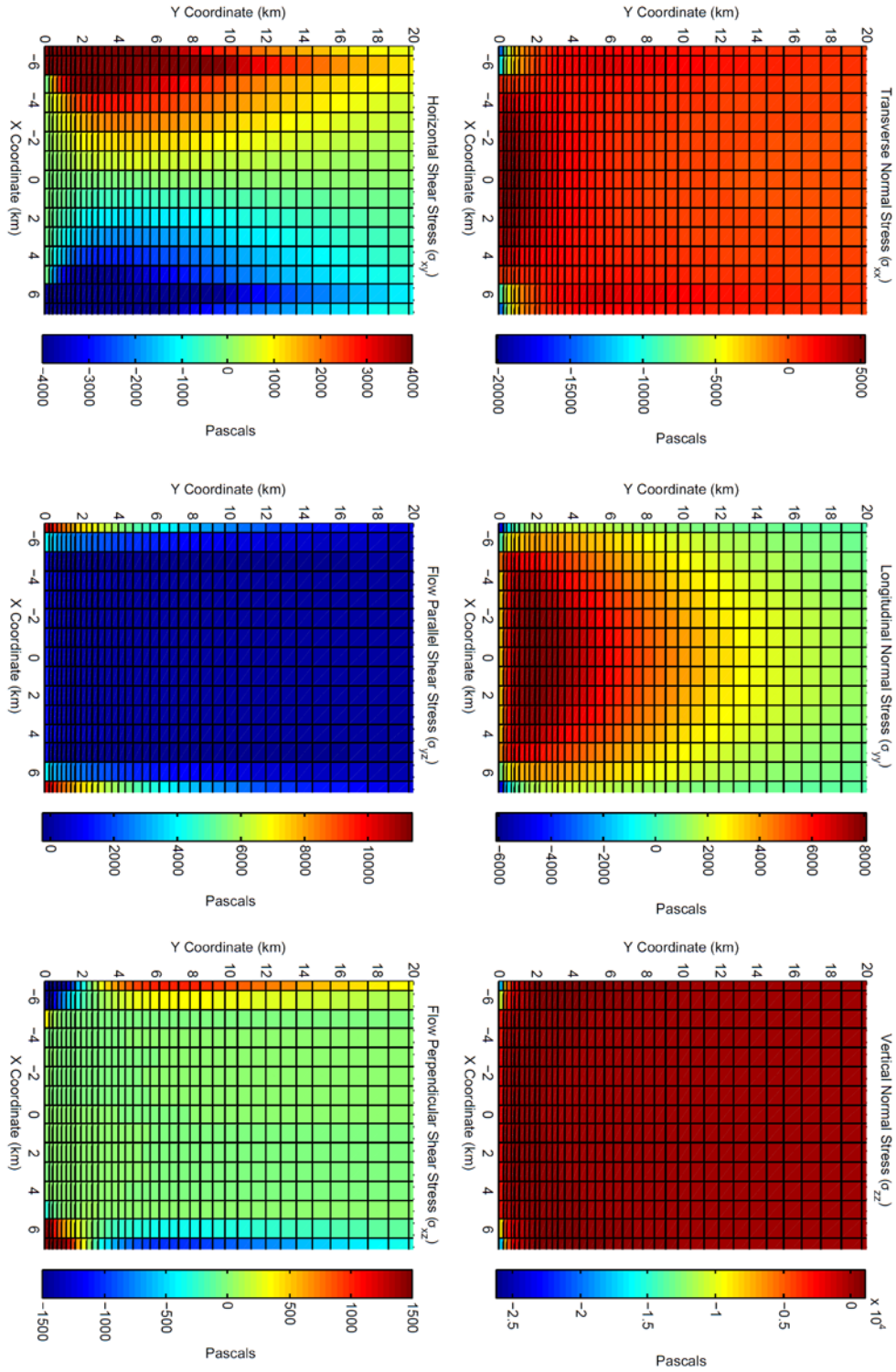

Figure 2D.5: Stress field for the three-dimensional model with *h=3 km, w=14 km,* and *E=9.33 GPa.*

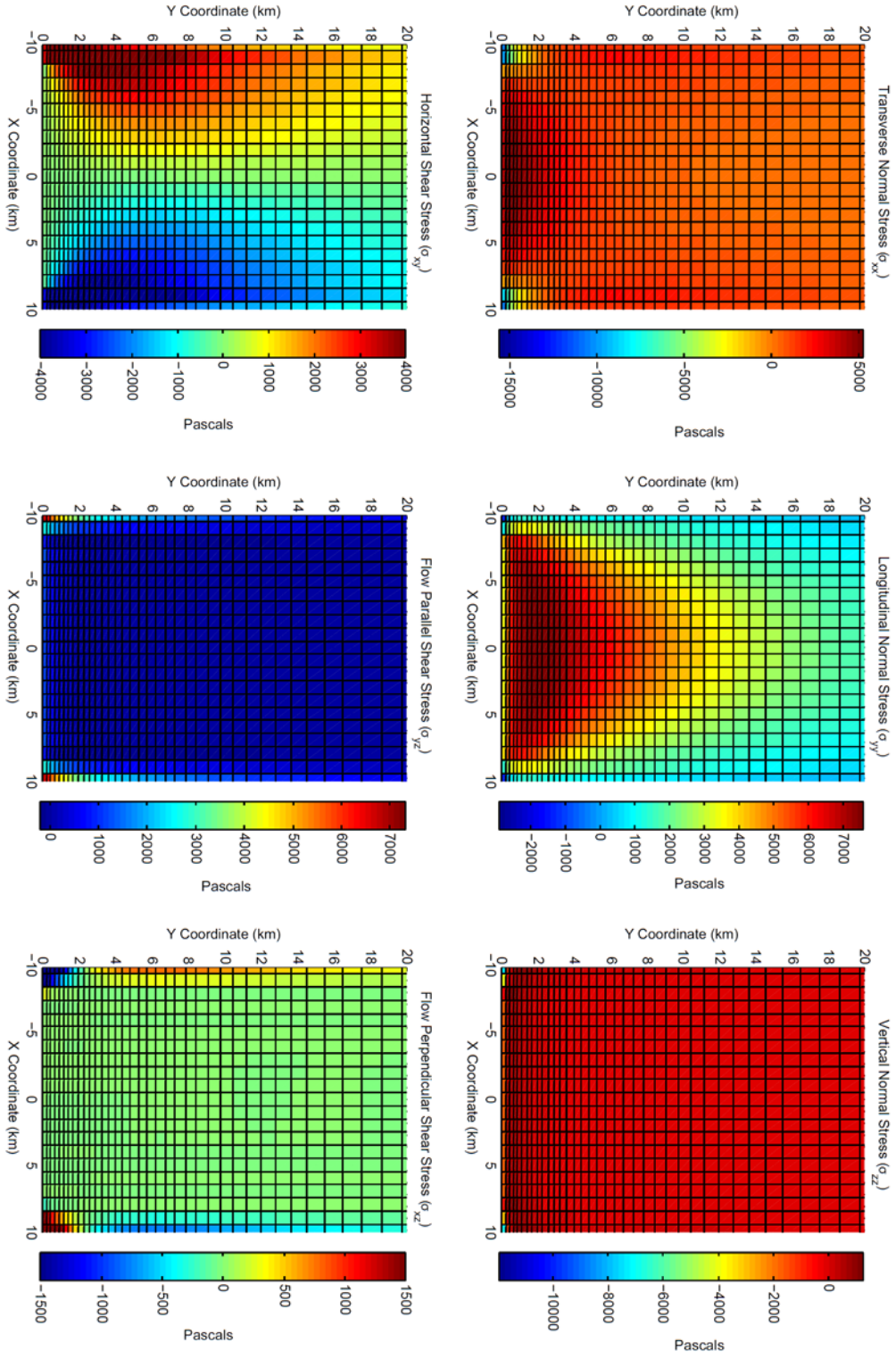

Figure 2D.6: Stress field for the three-dimensional model with *h=1 km, w=20 km,* and *E=9.33 GPa*.

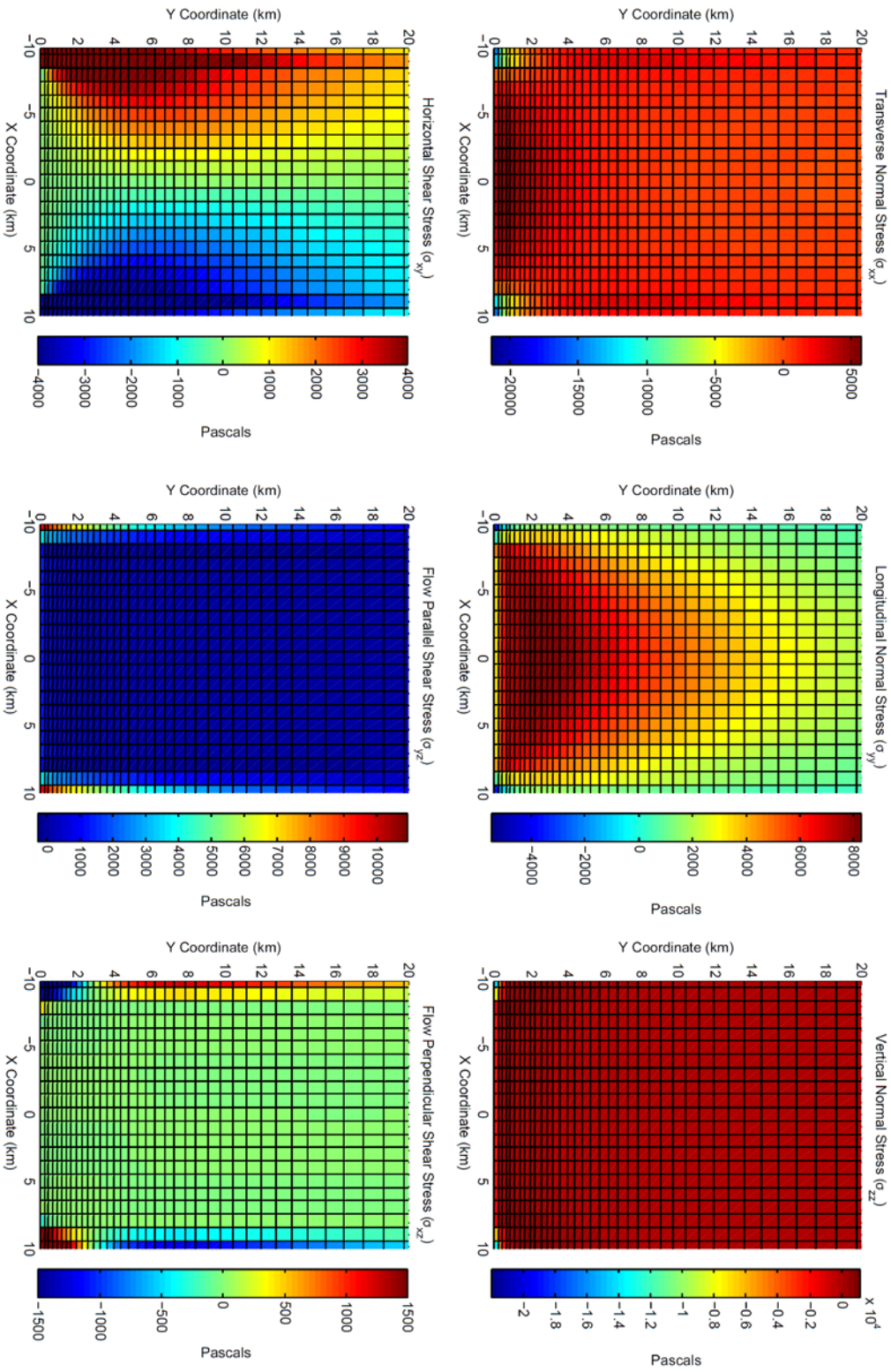

Figure 2D.7: Stress field for the three-dimensional model with *h=2 km*, *w=20 km*, and *E=9.33 GPa*.

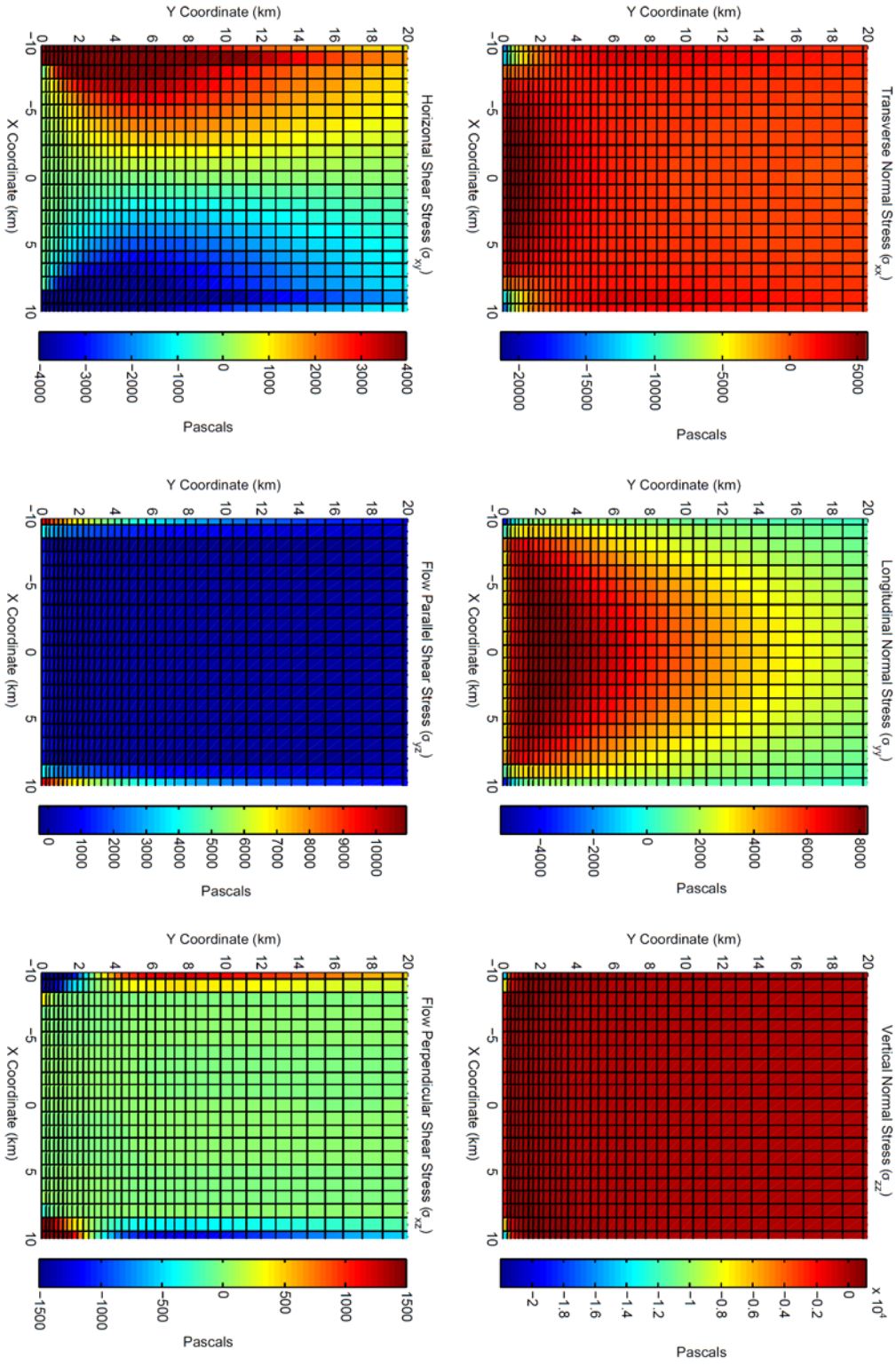

Figure 2D.8: Stress field for the three-dimensional model with *h=3 km*, *w=20 km*, and *E=9.33 GPa*.

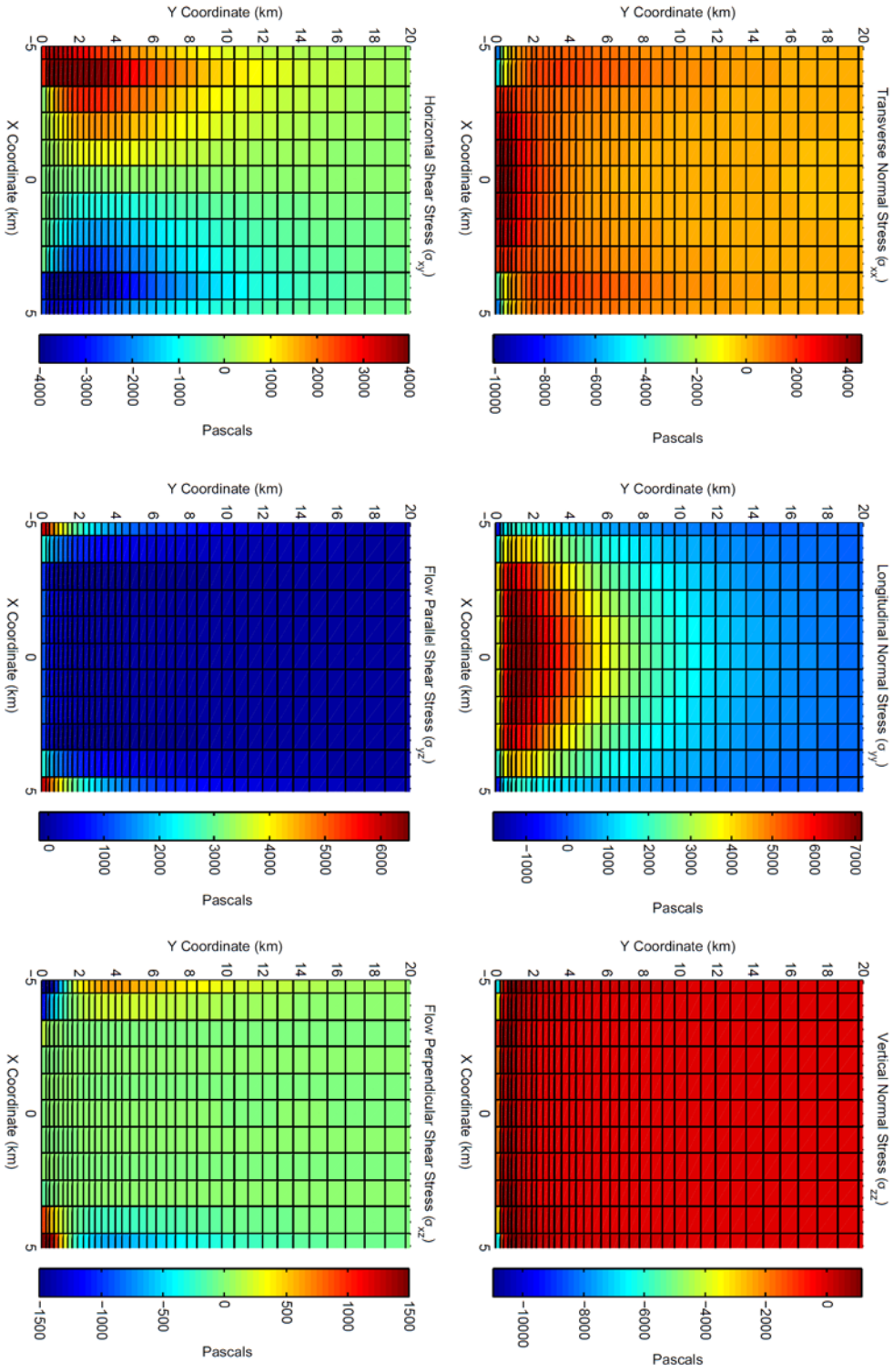

Figure 2D.9: Stress field for the three-dimensional model with *h=1 km*, *w=10 km*, and *E=0.933 GPa.*

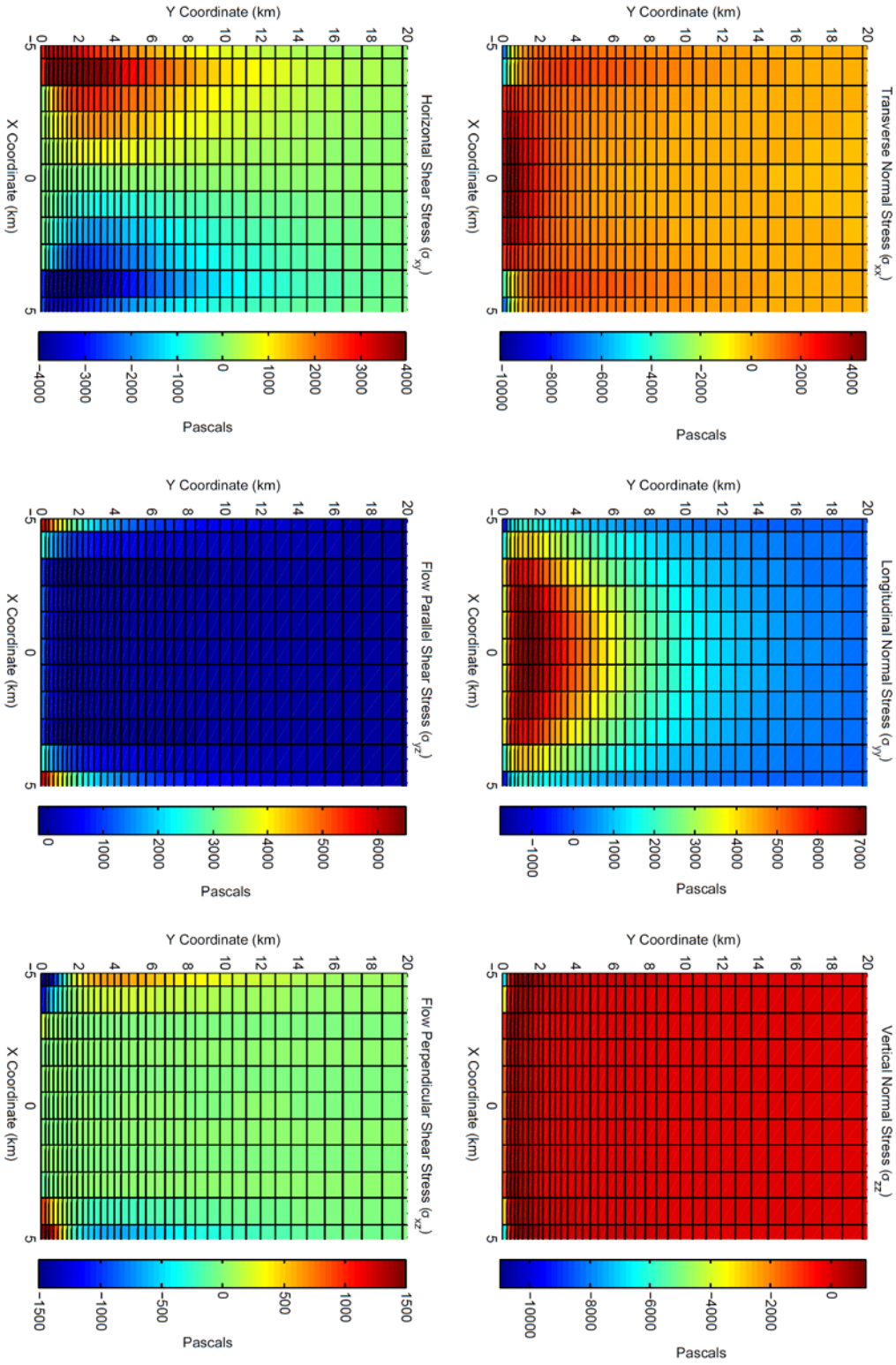

Figure 2D.10: Stress field for the three-dimensional model with *h=1 km*, *w=10 km*, and *E=93.3 GPa*.

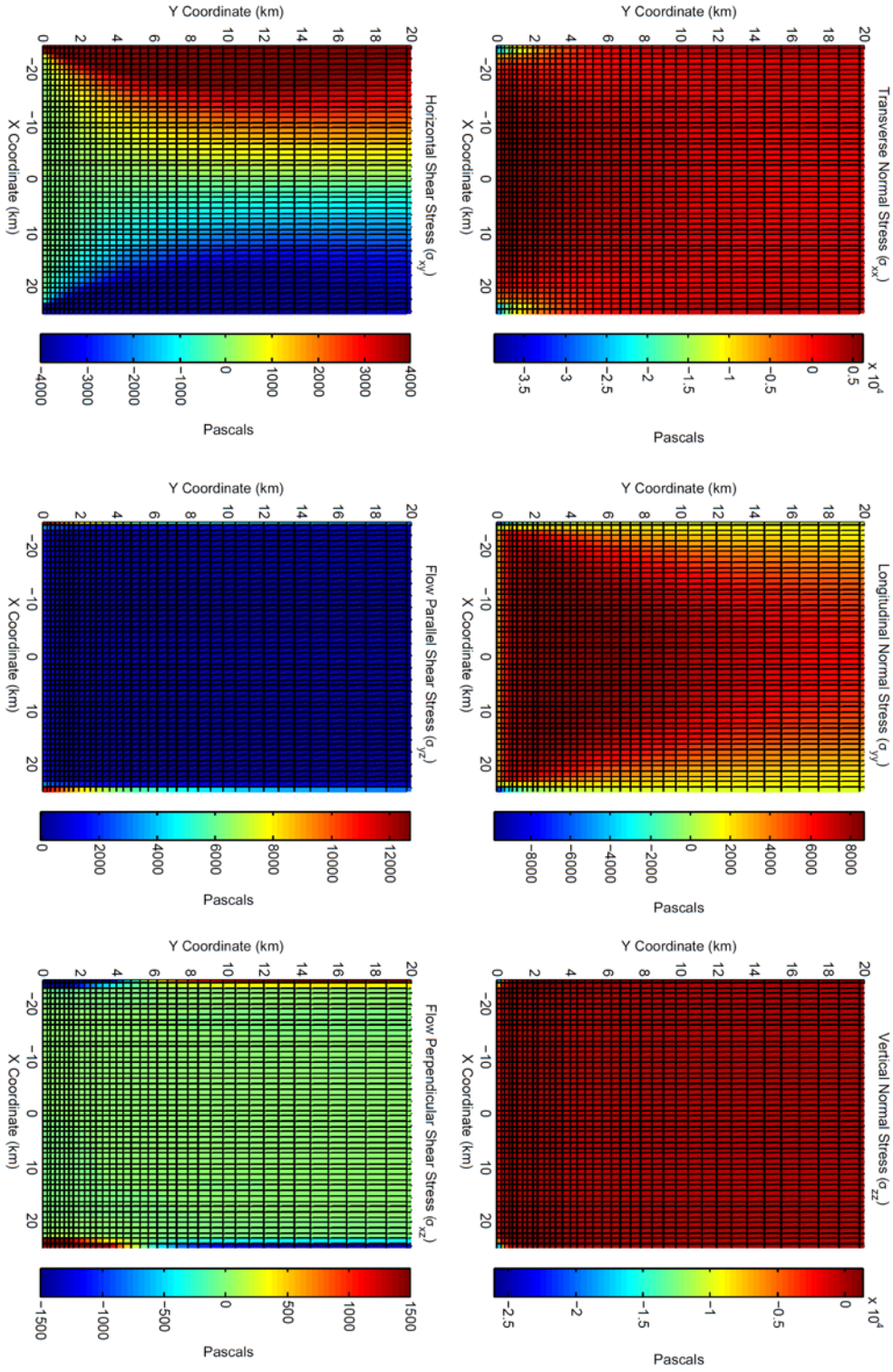

Figure 2D.11: Stress field for the three-dimensional model approximating Bindschadler Ice Stream, with *h=2 km, w=50 km,* and *E=9.33 GPa*.

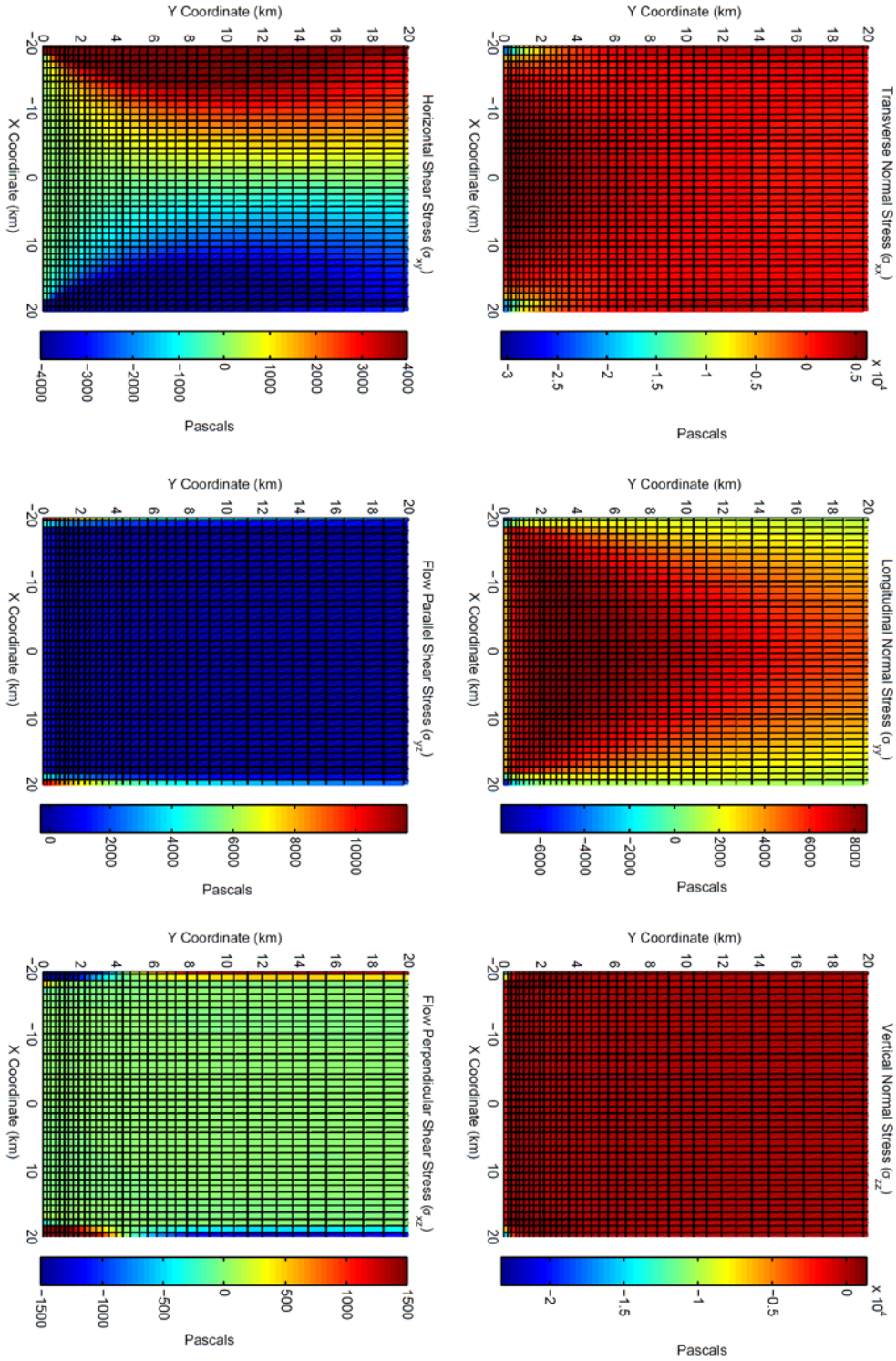

Figure 2D.12: Stress field for the three-dimensional model approximating Pine Island Glacier, with *h=2 km*, *w=40 km*, and *E=9.33 GPa*.

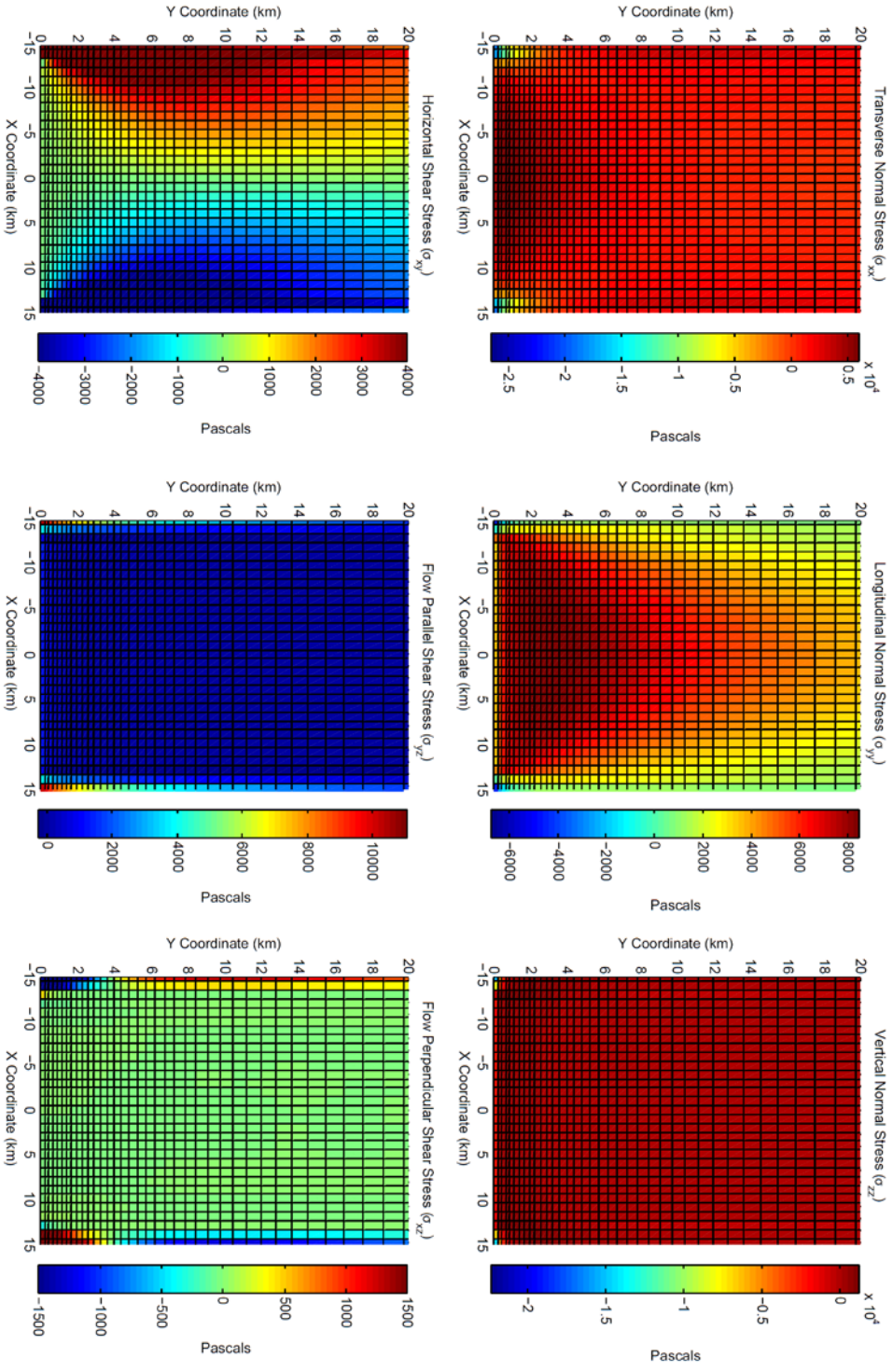

Figure 2D.13: Stress field for the three-dimensional model approximating Rutford Ice Stream, with *h=2 km*, *w=30 km*, and *E=9.33 GPa*.